Chapter 2

Aerodynamics Model

2.1 Background Information

The aerodynamics problem being dealt with as part of the design of MAGLEV vehicles is an exterior flow over a bluff body in close ground proximity. The target speed is 300 MPH which corresponds to a cruise Mach number of 0.4. In general, these vehicles experience flow separation on the last car as well as strong ground effect augmentation of the aerodynamic force and moment coefficients (lift reversal). As a body is brought closer to a ground plane the lift coefficient will initially decrease (and may even become negative) due to the Venturi effect. According to this largely inviscid phenomena, the flow must accelerate to travel through the thin gap between the vehicle and the ground plane, thereby lowering the pressure on the underside and reducing the lift. If the body is situated below a critical ground clearance, the lift will reverse and increase for any further reduction in the height above the ground plane. This is due to viscous effects which include a repositioning of the stagnation point and the separation lines whereby the lower portion of the separation line moves forward and the upper portion of the separation line moves aft. For flow over a body with a sharp trailing edge, lift reversal can involve flow separation on the lower surface. The problem of lift reversal is a difficult one to solve since it usually involves flow separation which has to be predicted by any flow solution method tackling the problem. Bearman [43] discusses some of these difficulties.

The prediction of reasonable force and moment coefficients is pivotal to the success of this shape optimization design, therefore much thought and work has gone into the development of this model. Aerodynamic analyses are developed for 2-D and 3-D flows. This chapter discusses the theoretical background for the aerodynamic models used for the design optimizations and also points out important implications these models make about the simulation of ground effect aerodynamics.

Aerodynamic analysis involves the solution of mass, momentum, and energy conservation equations.

$$\begin{aligned} \frac{\partial \rho}{\partial t} + \nabla \cdot \rho \mathbf{V} &= 0 \\ \rho \left(\frac{\partial V_i}{\partial t} + \mathbf{V} \cdot \nabla V_i \right) &= \rho f_i - \frac{\partial}{\partial x_i} \left(p + \frac{2}{3} \mu \nabla \cdot \mathbf{V} \right) + \frac{\partial}{\partial x_j} \mu \left(\frac{\partial V_i}{\partial x_j} + \frac{\partial V_j}{\partial x_i} \right) \\ \rho \frac{De}{Dt} + p \nabla \cdot \mathbf{V} &= \sum_{i=1}^{3} \frac{\partial}{\partial x_i} \left(k \frac{\partial T}{\partial x_i} \right) + \Phi(\text{Dissipation Function}) \end{aligned} \tag{2.1}$$

Although it only strictly refers to the conservation of momentum equations, this collection of equations is often referred to as the Navier-Stokes equations by the Computational Fluid Dynamics (CFD) community. In this discussion, we will be loose with this term and will specifically refer to momentum conservation when appropriate. Navier-Stokes calculations, especially subsonic ones, are computationally intensive and expensive in terms of CPU time. These calculations require both surface and volume grids with enough resolution to capture important flow phenomena. For the case of the MAGLEV vehicle, this would include the viscous flow in the gap between the vehicle and the track and that in the separation region. For turbulent flows, the Reynolds averaged form of these equations is used.

The difficulty presented by the problem size for Navier-Stokes calculations of MAGLEV vehicles is evident in the design work performed by Northrop Grumman Corporation [28]. The analysis of the full three dimensional vehicle with an elevated guideway required an 18 block grid with 1.1 million points for the half plane model. Twelve hundred multigrid cycles were needed to reduce the residual by three to four orders of magnitude. They were able to perform one such analysis and instead performed smaller three dimensional and two dimensional Navier-Stokes calculations for most of the design process. Similar calculations performed at NASA Ames Research

Center [44] were also costly, requiring a 12 block grid with 876,912 cells. It is abundantly clear that using Navier-Stokes analyses to analyze the flow over such vehicles within an optimization loop is too expensive and quite possibly implausible to automate at this time. Changes made to the surface geometry during an optimization loop might cause problems when mapping the grid, requiring manual repair.

Alternatively , the use of linear methods would require solely a surface grid and would require much less CPU time, making it more conducive for use in an MDO framework. The disadvantages of using such methods are that they cannot predict the effects of diffusion (skin friction and separation) and therefore rely on empirical relationships for this information. The advantages of using such methods are that boundary layer strip theory can provide reliable skin friction values, consistent separation criteria exist for two dimensional and axially symmetric turbulent flow, there is no need for the empiricism involved with turbulence models, they are easy to discretize, and fast to solve. It is for these reasons that the work presented here employs such methods.

Linear methods deal with the solution to Laplace's equation which results from several simplifying assumptions to the Navier-Stokes equations. Since the cruise Mach number is not high, the flow can be assumed incompressible. Since the density is then known throughout the flowfield there is no coupling of the energy conservation equation with those of mass and momentum conservation so the energy equation is not needed to uniquely determine the flowfield. Mass conservation is accomplished by maintaining that the velocity vector field is solenoidal.

$$\nabla \cdot \mathbf{V} = 0 \tag{2.2}$$

Assuming the flow is inviscid and irrotational, the continuity equation can be solved independently. The irrotational assumption allows the velocity vector to be derived from a scalar potential function, Φ, such that the gradient of Φ is the velocity vector. This is a result of the requirement that the circulation be zero for any arbitrary closed, reducible path in the fluid region. In order for this to be true, the integrand in the definition of circulation must be an exact differential. This can be seen in Eq.

2.3.

$$\begin{aligned}
\Gamma &= \oint_C \mathbf{V} \cdot dl = 0 \\
\Gamma &= \oint_C [udx + vdy + wdz] \\
&= \oint_C d\Phi \\
\Gamma &= \oint_C \left[\frac{\partial \Phi}{\partial x} dx + \frac{\partial \Phi}{\partial y} dy + \frac{\partial \Phi}{\partial z} dz \right] \\
\mathbf{V} &= \nabla \Phi
\end{aligned} \tag{2.3}$$

If the velocity vector is replaced in the continuity equation the resulting equation is Laplace's Eq. (2.4).

$$\nabla^2 \Phi = 0 \tag{2.4}$$

The flow can be completely determined based on mass conservation which involves one equation and one scalar unknown. The pressure field can then be found using the momentum equation (Bernoulli equation). Laplace's equation is a linear, homogeneous, partial differential equation. The analytic solutions to this equation are referred to as harmonic functions and can be linearly superimposed to satisfy the two boundary conditions.

Laplace's equation is solved by setting up a collection of these mathematically singular solutions on the solid boundaries of the flow. This separates the flow into two regions of potential flow (incompressible, irrotational, inviscid), one exterior to and one interior to a closed body. For our application, we will be concerned with the flow exterior to the boundary. This region is bounded by an interior boundary (the solid surface) and an exterior boundary at an infinite distance from the solid surface. The strengths of these functions are determined by imposing the aforementioned boundary conditions. This boundary condition is that of no-penetration of the fluid through the body surface and can be generally handled in one of two ways. The Neumann boundary condition is a direct implementation of no-penetration stating that the flow cannot have a velocity component normal to the boundary at the boundary surface. This condition is explicitly imposed at control points on the interior boundary and is

mathematically shown in Eq. 2.5.

$$\nabla\Phi \cdot \mathbf{n} = 0 \tag{2.5}$$

The harmonic functions automatically satisfy the no-penetration boundary condition at the infinity boundary. The Dirichlet boundary condition states that the no-penetration condition is equivalent to setting the potential inside the body described by the boundary to a constant. This boundary condition will be described in greater detail in the discussion of the doublet panel method for 2-D (Section 2.2.1) and 3-D flow (Section 2.3.1).

Another possible boundary condition is the no-slip condition which states that there is no relative tangential velocity between the solid and fluid at the boundary. It is generally not imposed for inviscid flows since the no-penetration condition on the two boundaries makes up the two necessary boundary conditions for the second order partial differential equation. The no-slip condition is mentioned here because it will be employed for the vortex panel method used in this work. It will be further discussed in Section 2.2.2 for the 2-D case and Section 2.3.3 for the 3-D case.

The formulation of the solution to Laplace's equation via the superposition of harmonic functions is different for lifting and non-lifting bodies. For non-lifting bodies, one can proceed with the solution without any additional information. On the other hand, the flow around lifting bodies cannot be calculated due to the implications of the irrotational assumption. Using Stokes Theorem with the irrotational flow assumption for a 3-D flow around a closed body in an infinite fluid region, one finds that the flow is acyclic ($\Gamma = 0$) and therefore cannot produce lift according to the Kutta-Joukowski theorem. For 2-D flow around an infinite cylinder of arbitrary cross section in an infinite fluid, the flow may or may not be cyclic, although the circulation is indeterminate. In order to calculate the flow around lifting bodies, auxiliary conditions are needed to uniquely determine the circulation around the body. These conditions are imposed in various ways but invariably stem from a condition on vorticity conservation.

Vorticity conservation conditions for incompressible flow with uniform density and

kinematic viscosity are shown in Eq. 2.6 for several different flow situations [45].

$$\begin{array}{ll} 3-D & \begin{cases} Viscous: \iiint_{R_\infty} \mathbf{\Omega} dR = 0 \\ Inviscid: \iiint_{R_f} \mathbf{\Omega} dR = 0 \end{cases} \\ 2-D & \begin{cases} Viscous: \frac{d}{dt} \iint_{R_\infty} \mathbf{\Omega} dR = 0 \\ Inviscid: \frac{d}{dt} \iint_{R_f} \mathbf{\Omega} dR = 0 \end{cases} \end{array} \tag{2.6}$$

These conditions stem from conservation of angular momentum. Their derivation along with a brief discussion can be found in Appendix A. All of the conditions shown here are in terms of the integral of vorticity over a region. R_f refers to the fluid region and R_∞ refers to the combined fluid and solid regions. For viscous flow cases, the integral of vorticity over the combined solid/fluid region is always a constant. For three dimensional flow, this constant is always zero, while for two dimensional flow this constant is zero if the flow begins from rest. Since this condition is imposed over the entire region, R_∞, it provides a relationship between the vorticity in the fluid and the vorticity of the solid regions which is two times the angular velocity of the solid body rotation. This vorticity is transported across the solid boundary via the no-slip condition. The vorticity diffuses and convects into the fluid region in such a way as to obey the equations of motion and the boundary conditions.

The vorticity conservation conditions for the inviscid flow cases closely resemble the vorticity conservation conditions for viscous flow except the integral excludes the solid regions. This is a result of the absence of a no-slip condition, so vorticity associated with the angular velocity of the solid regions cannot be transported across the solid boundaries. The difference between this condition and that for the viscous case is a crucial one which has a large impact on the solution to many flowfields, especially unsteady ones. For an obvious example, one can look at the 2-D flow around an airfoil oscillating in pitch. If Eq. A.24 is used as the vorticity conservation condition and the problem is impulsively started, then the integral of the vorticity throughout the fluid region will be zero for all time. If Eq. A.22 is used as the vorticity conservation condition and the problem is impulsively started, then the integral of the vorticity over the fluid region is equal to the negative of two times the angular velocity of the pitching airfoil. The latter case for this example is closer to reality

and can be implemented as a conservation condition even if the inviscid assumption is made (diffusion of vorticity is ignored). In doing so ,the mechanics of the creation of vorticity at a solid boundary is properly modeled.

The correct implementation of these vorticity conservation conditions is essential for properly modeling flows as will be shown in the following sections of this chapter. These conditions are both imposed explicitly and used to determine a shedding rate for the convection of vorticity away from the solid bodies.

A brief description of the nature of real flows over solid bodies is useful here. Flow will attach itself to a solid body at an upstream attachment point and remain attached to the solid surface until it reaches a line of separation. Vorticity is created at the solid boundary between the attachment point and separation line and is carried away from the solid surface by diffusion. Vorticity is also carried into the fluid region by convection from the separation lines. This process is discussed in greater detail in Ref. [46].

The locations of attachment and separation points along with the shedding rates at the separation locations determine the circulation around the solid body and, therefore, the forces and moments on that body. For 2-D flows over bodies with sharp trailing edges, there is an attachment point near the leading edge, a separation point at the trailing edge and possibly other separation and attachment points depending upon the angle of attack. For 2-D bluff body flows there is an attachment point near the leading edge and two separation points which form the boundary for a separation "bubble" at the aft portion of the body. For bluff body flow, there is also the possibility for additional localized separations and reattachments. The corresponding 3-D flows involve separation lines which can form closed curves for the bluff body case. The 2-D cases can be seen in Fig. 2.1 which is a replication of a figure from Ref. [46].

For the case of linear aerodynamics, the shedding rates can be determined by using the vorticity conservation condition and an auxiliary condition which describes the nature of the flow at the separation locations. For attached flow over sharp trailing edge bodies, this additional condition which is applied at the trailing edge is the well-known Kutta condition. The Kutta condition states that the circulation is set to make the flow leave an airfoil smoothly at the sharp trailing edge (Ref. [47]). The proper

implementation of the Kutta condition is different for steady and unsteady flow. A comparable condition exists for bluff body separation and can only be implemented in an unsteady fashion.

Some implications of the vorticity theory on the flow problem at hand are worth mentioning here, prior to their discussion in the appropriate sections. The first is that vorticity conservation conditions will dictate the type of solution process needed for the analysis of the flow. For example, a 2-D flow over a body with a single separation point will shed vorticity during unsteady motion only. On the other hand, a 2-D, separated flow over a bluff body always sheds vorticity, so the solution for the flow around such bodies using linear methods must always be solved in an unsteady fashion to allow for the proper wake development. Similarly, for 3-D flows over bodies with sharp trailing edges and 3-D, separated flows over bluff bodies, vorticity is always shed. These flows must also be solved in an unsteady fashion. An unsteady solution means that the flow is solved over successive time steps during which the wake is developed. At each individual time step, the flow is solved in the same steady fashion since the governing equation is elliptic.

The second implication is that linear aerodynamic predictions can detect phenomena normally attributed to high-order aerodynamics if the flow mechanics are properly modeled. This has been demonstrated already in the use of the Kutta condition and vorticity conservation. Laplace's equation is purely kinematic, so in order to predict lifting flows the necessary kinetics are embodied in the auxiliary conditions. Other examples of this are given in a review article by Leonard ([33]). One impressive example uses discrete vortices to model a viscous boundary layer. The vortices are formed at the solid surface and are free to convect and required to diffuse (using a time varying vortex blob diameter) in order to satisfy the viscous vorticity transport equation. An image method is used to assure no-penetration and the discrete vortex strengths are determined to satisfy the no-slip condition. Such a method can be converged to the Navier-Stokes solution to the flow and can even accurately predict flow separation. In Section 2.2, we show the importance of properly modeling the mechanics of a flow for the case of ground effect aerodynamics.

2.2 2-D Model

This section considers two different models which are referred to as the "Doublet Panel Method" (DPM) and the "Vortex Panel Method" (VPM). They are described in detail in their respective subsections and then compared to illustrate the importance of properly modeling the mechanics for ground effect aerodynamics.

The doublet panel method is formulated from the solution to Laplace's equation based on Green's Identity. The vortex panel method is based on a model described by Mook and Dong in Ref. [36]. Both of the methods are extended here for flow around a bluff body and for ground effect aerodynamics. It is shown that the vortex panel method is kinematically closer to a real flow and is able to predict some aspects of viscous flow which are normally attributed only to higher-order models.

The vortex panel method is used for all of the 2-D optimizations. Extensions are made to include some aspects of viscous flow. These extensions include a turbulent flow separation criterion and a model for the base pressure in the separation bubble for bluff body calculations. Skin friction is calculated along the solid surface from the stagnation point (attachment) to the separation points using boundary layer integral methods and a transition criterion. A separate viscous flow model was developed for the lower surface of bluff bodies in ground effect. This model is a turbulent Couette/Poiseuille flow calculation which can calculate the fully developed, 2-D, parallel flow between flat plates with one moving wall, one stationary wall, and a pressure gradient. Each model is described in its own subsection below.

2.2.1 Doublet Panel Method

As was previously mentioned, linear methods deal with the solution of Laplace's equation. The doublet panel method involves the solution based on Green's Identity [48]. Green's Identity is the divergence theorem written for a vector composed of two scalar functions of position, $\Phi_1 \nabla \Phi_2 - \Phi_2 \nabla \Phi_1$. If we set $\Phi_1 = \ln \mathbf{r}$ and $\Phi_2 = \Phi$ the components of the Green's Identity resemble distributed sources and doublets with the strengths σ and μ respectively. An overview of this formulation can be found in Appendix D. The no-penetration boundary condition is imposed implicitly using

the Dirichlet boundary condition. This states that imposing no-penetration explicitly is equivalent to setting the potential inside the solid surface equal to a constant or to the free stream potential, ϕ_∞. The simulation of ground effect is accomplished using the method of images which is described in greater detail in Section 2.2.5. The aforementioned distributed doublet is mathematically equivalent to discrete vortices at the panel nodes. This discrete vorticity is not kinematically identical to a real flow which has continuous vorticity being created at the solid surface.

This model is capable of handling sharp trailing edge flow and bluff body flow. It accomplishes this by incorporating both steady and unsteady auxiliary conditions for the separation lines. For flows over bodies with sharp trailing edges, there is no vortex shedding for steady state flow. The trailing edge condition specifies that the circulation at the trailing edge be zero (stagnation point). This is accomplished using Eq. 2.7 which sets the panels adjacent to the trailing edge to equal strength.

$$\begin{aligned} \Gamma_{TE} &= 0 \\ \mu_U - \mu_L &= 0 \end{aligned} \tag{2.7}$$

The subscripts refer to "upper" and "lower" respectively. For bluff body separation or unsteady sharp trailing edge vortex shedding, an unsteady auxiliary condition is necessary. This condition stems from the vorticity conservation condition for 2-D, inviscid flow (Eq. 2.6). This condition requires that $\frac{d\Gamma}{dt} = 0$ so the time rate of change of circulation around the solid body is the negative of that in the wake. Therefore, the circulation at the separation line is that which is entering the wake. Equation 2.8 shows how this condition is used to set the strength of the wake doublet panel shed at time, t.

$$\begin{aligned} \frac{d\Gamma}{dt} &= \frac{d\Gamma_B}{dt} + \frac{d\Gamma_w}{dt} = 0 \\ \frac{\Delta\Gamma_{TE}}{\Delta t} &= \frac{(\mu_U - \mu_L)_t - (\mu_U - \mu_L)_{t-\Delta t}}{\Delta t} \\ \mu_w &= (\mu_U - \mu_L)_{t-\Delta t} \end{aligned} \tag{2.8}$$

The wake of doublet panels convect with the local velocity so as to remain force free. The baseline code for the one used here was one from Katz and Plotkin (Ref. [48]).

2.2.2 Vortex Panel Method

The vortex panel method is described in Ref. [36] and will be outlined here for the reader's convenience. This method has strong parallels to boundary layer theory so it is enlightening to begin the description by juxtaposing the two approaches. The boundary layer assumptions state that the Reynolds number is very large so that the viscous effects are confined to a small region bordering the solid surface. Along with an assumption of modest surface curvature, the boundary layer equations describe the viscous flow as being forced by the pressure at the boundary layer edge which can be determined using linear methods. The vortex panel method makes similar assumptions and takes an opposite approach, that the vorticity in the viscous regions determines the flow in the inviscid region through a kinematic relationship.

A kinematic relationship between vorticity and velocity can be determined simply using the continuity equation for an incompressible flow and the definition of vorticity. This relation is shown in Eq. 2.9 and is derived in Section 18.6 of Ref. [47].

$$\mathbf{V}(\mathbf{r},t) = \frac{1}{2\pi}\iint_{S_\infty} \frac{\mathbf{\Omega}(\mathbf{r_o},t)\times(\mathbf{r}-\mathbf{r_o})}{|\mathbf{r}-\mathbf{r_o}|^2} dS(\mathbf{r_o}) + \mathbf{V}_\infty \tag{2.9}$$

Figure 2.2 shows the arrangement of vectors in Eq. 2.9. Equation 2.9 states that the velocity at a point in the flow is composed of the uniform free stream flow and the sum of the perturbations from the vortical fluid elements. This perturbation term is the Biot Savart law. Since this kinematic relation was derived solely using continuity and the definition of vorticity, it holds for both viscous and inviscid flows. The flow induced by the viscous boundary layer can therefore be described using the perturbation term of Eq. 2.9. This can be seen in Eq. 2.10.

$$\mathbf{V}_B(\mathbf{r},t) = \frac{1}{2\pi}\iint_{S_B} \frac{\mathbf{\Omega}(\mathbf{r_o},t)\times(\mathbf{r}-\mathbf{r_o})}{|\mathbf{r}-\mathbf{r_o}|^2} dS(\mathbf{r_o}) \tag{2.10}$$

If we integrate Eq. 2.10 with respect to the boundary layer thickness and take the limit of the Reynolds number approaching infinity while the boundary layer thickness approaches zero we obtain Eq. 2.11.

$$\mathbf{V}_B(\mathbf{r},t) \;=\; -\frac{1}{2\pi}\mathbf{e}_z \times \oint_c \frac{\gamma[l(\mathbf{r_o}),t](\mathbf{r}-\mathbf{r_o})}{|\mathbf{r}-\mathbf{r_o}|^2} dl(\mathbf{r_o})$$

where

$$\gamma(l,t)\mathbf{e}_z = \lim_{\substack{Re\to\infty \\ \delta\to 0}} \left[-\int_0^{\delta(l)} \mathbf{\Omega}(l,n,t)dn \right] \tag{2.11}$$

So, for very high Reynolds number ($Re \to \infty$) the boundary layer can be approximated by a continuous vortex sheet. This assumption infers that convection of vorticity is infinitely faster than diffusion of vorticity (inviscid flow). This vortex sheet is a solution to Laplace's equation, so the solution will proceed accordingly. Since the vorticity is the curl of the velocity vector and there is no normal velocity at the surface, the vortex sheet strength, γ, described in Eq. 2.11 is the difference in tangential velocity across the sheet.

$$\begin{aligned} \gamma(l,t) &= \lim_{\substack{Re\to\infty \\ \delta\to 0}} \left[\int_0^{\delta(l)} \frac{\partial u}{\partial n} dn \right] \\ &= u(l,0^+,t) - u(l,0,t) \\ &= \Delta u(l,t) \end{aligned} \tag{2.12}$$

If we now apply the no-slip condition ($u(l,0,t) = 0$) the strength of the vortex sheet is equal to the tangential velocity at the edge of the infinitely thin boundary layer.

$$\gamma(l,t) = u(l,0^+,t) \tag{2.13}$$

The flow outside the infinitely thin boundary layer "slips" over the solid surface where the velocity is discontinuous. The inviscid assumption ($Re \to \infty$) is kinematically identical to the impulsively started viscous flow over the solid body in the limit as time approaches zero. At that instant, all of the vorticity generated during the impulsive start resides in an infinitely thin sheet at the solid surface. For the viscous case, as time proceeds this vorticity diffuses into the flow creating the boundary layer. It is this kinematic similarity to viscous flow which allows this model to predict ground effect flow more accurately than the doublet panel method, as will be demonstrated later.

Since we are neglecting diffusion, convection is the only mechanism for the transport of vorticity. As was previously discussed in this chapter, convection occurs from separation points only and can therefore be determined by vorticity conservation conditions. The derivation of this vortex panel method is concerned with flow

over bodies with sharp trailing edges. Flows over bluff bodies will be discussed in a separate section on the extension of this model to that case.

For flow over bodies with sharp trailing edges, we have already stated that the circulation is set such that flow leaves the trailing edge smoothly (Kutta condition). This is implemented here by requiring that the pressures match at the upper and lower surfaces of the trailing edge. Since the flow is inviscid, Euler's equation (momentum conservation) can be used to relate the velocity to the pressure. Euler's equation is shown (Eq. 2.14) here where l is the tangential direction around the surface of the airfoil.

$$\frac{\partial \gamma}{\partial t} + \gamma \frac{\partial \gamma}{\partial l} = -\frac{1}{\rho}\frac{\partial P}{\partial l} \tag{2.14}$$

Multiplying across by dl and integrating around the airfoil from the lower surface of the trailing edge, L, to the upper surface of the trailing edge, U, gives Eq. 2.15.

$$\begin{aligned} \frac{\partial \gamma}{\partial t} dl + \gamma d\gamma &= -\frac{1}{\rho} dP \\ \frac{d}{dt}\left[\oint_c \gamma(l,t) dl\right] + \frac{\gamma^2}{2}\Big|_L^U &= -\frac{1}{\rho} P\Big|_L^U \end{aligned} \tag{2.15}$$

Figure 2.3 shows the path of integration. The integral on the left hand side is the definition of the circulation around the solid body, so Eq. 2.15 can be rewritten as shown in Eq. 2.16.

$$\frac{d\Gamma(t)}{dt} + \frac{\gamma_U^2 - \gamma_L^2}{2} = -\frac{1}{\rho}(P_U - P_L) \tag{2.16}$$

Imposing the Kutta condition such that the pressure is equal across the trailing edge ($P_U = P_L$) one concludes that the rate of change of circulation in the flow is a function of the tangential velocity at the upper and lower surfaces of the trailing edge (Eq. 2.17).

$$\frac{d\Gamma(t)}{dt} = \frac{\gamma_L^2 - \gamma_U^2}{2} \tag{2.17}$$

The vorticity conservation condition for 2-D flow (Eq. 2.6) is rewritten in Eq. 2.18 in terms of the circulation ($\Gamma(t)$).

$$\frac{d\Gamma}{dt} - 2\dot{\theta} S_S + \frac{d\Gamma_w}{dt} = 0 \tag{2.18}$$

This is the conservation condition for viscous flow, so the circulation includes a term for the solid body rotation of the solid region at an angular velocity, $\dot{\theta}$. We are not dealing with these flows specifically here so this term will be dropped from the present derivation. It can always be added in later. Substituting Eq. 2.17 into Eq. 2.18, one arrives at the vortex shedding rate for the convection of vorticity from the separation point at the trailing edge into the fluid region (Eq. 2.19).

$$\begin{aligned} \frac{d\Gamma_w}{dt} &= -\frac{d\Gamma}{dt} \\ &= \frac{\gamma_U^2 - \gamma_L^2}{2} \end{aligned} \tag{2.19}$$

Observations of the flow at the trailing edge provide additional necessary information to include along with the vortex shedding rate equation. For this information, we use the Giesing/Maskell model for the trailing edge flow [37] [38]. The statement of this model (Eq. 2.20) discusses the possible values of the trailing edge velocities (sheet strength) depending upon the value of the derivative of the circulation.

$$\begin{aligned} \frac{d\Gamma}{dt} > 0 \quad & \begin{cases} \gamma_L \neq 0 \\ \gamma_U = 0 \end{cases} \\ \frac{d\Gamma}{dt} = 0 \quad & \begin{cases} \gamma_L = 0 \\ \gamma_U = 0 \end{cases} \\ \frac{d\Gamma}{dt} < 0 \quad & \begin{cases} \gamma_L = 0 \\ \gamma_U \neq 0 \end{cases} \end{aligned} \tag{2.20}$$

If the flow is unsteady and $\frac{d\Gamma}{dt}$ is positive, the flow over the bottom of the airfoil leaves the trailing edge at γ_L, while the flow over the top of the airfoil meets a stagnation point at the trailing edge. If the flow is unsteady and $\frac{d\Gamma}{dt}$ is negative, the flow over the top of the airfoil leaves the trailing edge at γ_U, while the flow over the bottom of the airfoil meets a stagnation point at the trailing edge. If the flow is steady, the flow over the top and bottom surfaces of the airfoil both meet a stagnation point at the trailing edge. So, for the 2-D flow over a body with a sharp trailing edge, vorticity is shed (convected) into the flow only if the flow is unsteady.

The amount of circulation added to the wake in a time step, Δt, follows from Eq.

2.19 and the Giesing/Maskell model and is shown in Eq. 2.21.

$$\begin{aligned} \Delta\Gamma_w &= \tfrac{\gamma_U^2}{2}\Delta t \quad \tfrac{d\Gamma}{dt} < 0 \\ \Delta\Gamma_w &= -\tfrac{\gamma_L^2}{2}\Delta t \quad \tfrac{d\Gamma}{dt} > 0 \end{aligned} \tag{2.21}$$

The wake is constructed using a collection of discrete vortices where one discrete vortex is released from the trailing edge during each time step. The circulation around the wake is simply the summation of the strength of all of the discrete vortices that comprise the wake, where the strength of each discrete vortex is $\Delta\Gamma_w(t_k)$ (Eq. 2.22).

$$\Gamma_w = \sum_{k=1}^{M} \Gamma_k \tag{2.22}$$

The velocity induced by the wake can be calculated using the Biot-Savart law. This velocity is shown in Eq. 2.23 where σ signifies the radius of the vortex blob [36].

$$\mathbf{V}_w(\mathbf{r}, t) = -\frac{1}{2\pi}\mathbf{e}_z \times \sum_{k=1}^{M} \Gamma_k \frac{\mathbf{r} - \mathbf{r}_k}{|\mathbf{r} - \mathbf{r}_k|^2 + \sigma^2} \tag{2.23}$$

The vortex blob method is employed here to combat instabilities in the solution which can be created by the free convection of singular functions. The method will be described in Section 2.2.3.

The flow solution is obtained as a linear superposition of the continuous vortex sheet (modeling the boundary layer), discrete vortices (modeling the wake) , and the uniform free stream flow (all of which are solutions to Laplace's equation) in such a way as to satisfy the no-penetration boundary condition of the Neumann type (Eq. 2.24).

$$(\mathbf{V}_B + \mathbf{V}_w + \mathbf{V}_\infty) \cdot \mathbf{n} = 0 \tag{2.24}$$

The boundary condition is met at successive time steps with a discrete vortex shed into the flow at the end of each one. Each discrete vortex of the wake is convected at the local velocity which is induced by the vortex sheet representing the bound vorticity in the boundary layer and the other discrete vortices of the wake.

The pressures over the surface are calculated using the unsteady Bernoulli equation (Eq. 2.25).

$$\frac{\partial\phi}{\partial t} + \frac{1}{2}V^2 + \frac{p}{\rho} = \quad \text{Constant} \tag{2.25}$$

The aerodynamic forces and moments are determined by integrating the pressures around the airfoil. The specifics of the discretization of the airfoil and the problem setup and solution can be seen in Appendix B.

2.2.3 Vortex Blob Method

As previously stated, the vortex panel method sheds a wake which is modeled by discrete vortices. Since the vortex sheet is not a solid surface, it cannot support a force. Keeping the sheet force-free is accomplished by convecting each discrete vortex with the local velocity. The local velocity at each free vortex is the summation of the velocity induced by the free stream, continuous vortex sheet, and other free vortices. Since the vortices are mathematically singular, close proximity between vortices will result in very large velocities and they will propel each other far from the field of interest during a time step. Equation 2.9 shows that as $\mathbf{r}$ approaches $\mathbf{r_o}$ the induced velocity approaches infinity. Leonard (Ref. [33]) discusses the convection of discrete vortices and points out that this instability in the solution is inevitable if enough time steps are taken. This problem can be lessened with the use of vortex "blobs," which are vortices with finite cores. The induced velocities in the finite cores are described by distribution functions. The Biot-Savart law can be augmented with a function, $g(d)$, as is shown in Eq. 2.26.

$$\begin{aligned} \mathbf{V}(\mathbf{r},t) &= -\frac{1}{2\pi}\sum_{k=1}^{M}\frac{(\mathbf{r}-\mathbf{r_k})\times\mathbf{e}_z\Gamma_k g(d)}{|\mathbf{r}-\mathbf{r_k}|^2} \\ d &= \frac{|\mathbf{r}-\mathbf{r_k}|}{\sigma_k} \end{aligned} \tag{2.26}$$

The parameter, σ, is the radius of the vortex blob. Leonard (Ref. [33]) describes a Gaussian distribution function of the form shown in Eq. 2.27.

$$F(d) = \frac{e^{-d^2}}{\pi} \tag{2.27}$$

The function g can then be calculated as

$$\begin{aligned} g(d) &= 2\pi\int_0^d F(d')d'dd' \\ &= 1-e^{-d^2} \end{aligned} \tag{2.28}$$

This distribution function eliminates the mathematical singularity at $\mathbf{r} = \mathbf{r_k}$ and allows for a more stable solution.

A plot of the induced velocity for the vortex blob with a Gaussian distribution can be seen in Fig. 2.4. The vortex panel method used in this research has a wake vortex induced velocity shown in Eq. 2.23 which results from the distribution in Eq. 2.29.

$$g(d) = \frac{d^2}{1 + d^2} \tag{2.29}$$

It is obvious from Eq. 2.23 that a non-zero vortex blob radius would eliminate the singularity at $\mathbf{r} = \mathbf{r_k}$. A plot of the induced velocity for the vortex blob with the distribution of Eq. 2.29 can be seen in Fig. 2.5. The radius of the vortex blobs should be chosen according to the nominal separation of vortices in the shed wake. If we say that the nominal separation is some multiple of the free stream velocity and the time step, σ can be obtained by trial and error being the lowest possible value to yield a stable solution. For this work, σ is given in Eq. 2.30 where the constant, σ', is adjusted from case to case.

$$\sigma = \sigma' V_\infty \Delta t \tag{2.30}$$

2.2.4 Extension for Bluff Body Aerodynamics

For the 2-D flow over a bluff body, the flow has two separation points as opposed to the single separation point at a sharp trailing edge. It will, therefore, have two attachment points (the stagnation point and an attachment point in the wake). This can be seen in Fig. 2.1. The model for the bluff body, therefore, has to deal with two shedding rates, since vorticity is convected away at the two separation points. To do this, we must look at the flow near a separation point as sketched in Fig. 2.6. Reference [37] uses the unsteady Bernoulli equation (Eq. 2.25) to determine the vorticity shedding rate by treating the vortex sheet as a flow discontinuity in terms of the pressure, velocity, pressure head, and velocity potential.

Since we are not dealing with a multienergy flow, the pressure head is a constant throughout the flowfield. The bluff body analogue to the Kutta condition is that the pressure on both sides of the shed vortex sheet near the separation point is equal.

This will give Eq. 2.31 where the Δ refers to the discontinuity across the separation streamline and the $\bar{V}$ refers to the velocity of the separation streamline (average of the velocity on either side of the separation streamline).

$$\bar{V}\Delta V = -\frac{\partial \Delta\phi}{\partial t} \tag{2.31}$$

This equation is a parallel to Eq. 2.17 for the sharp trailing edge case.

If one ignores entrainment in the separation bubble, the circulation around the solid body can be related to the potential jump across the two vortex sheets which comprise the wake.

$$\Gamma = \Delta\phi_2 - \Delta\phi_1 \tag{2.32}$$

The subscript "1" refers to the lower separation point and the subscript "2" refers to the upper separation point according to Fig. 2.6. Equation 2.32 along with Eq. 2.31 describes the rate of change of the circulation as a function of the velocity on either side of the two wake vortex sheets (see Eq. 2.33).

$$-\frac{d\Gamma}{dt} = \left.\frac{\gamma_U^2 - \gamma_L^2}{2}\right|_2 - \left.\frac{\gamma_U^2 - \gamma_L^2}{2}\right|_1 \tag{2.33}$$

The subscript "U" refers to just upstream of the separation point and the subscript "L" refers to just downstream of the separation point. These subscripts are held over from those used in the sharp trailing edge Giesing/Maskell model. Their use here is consistent with the sign of the shed vortex strength. So, according to vorticity conservation, Eq. 2.18, the vortex shedding rate for the entire wake (upper and lower sheets) is

$$\frac{d\Gamma_w}{dt} = \left.\frac{\gamma_U^2 - \gamma_L^2}{2}\right|_2 - \left.\frac{\gamma_U^2 - \gamma_L^2}{2}\right|_1 \tag{2.34}$$

This is simply the sum of the shedding rates at the two separation points.

It can be argued that in order to have a bluff body separation bubble the shedding rates at each separation point cannot be zero (as was the case for the steady flow over a body with a sharp trailing edge). So, for the 2-D flow over a bluff body, vorticity is always shed into the flow. The flow is never actually steady, therefore it must be solved in a time dependent fashion. The flow will reach a quasi-steady state in which the circulation around the solid body is steady in the mean. The actual value will

continue to oscillate slightly about the mean due to an instability in the separation location and the periodic nature of vortex shedding. At this quasi-steady state, Eq. 2.35 will hold in the mean.

$$\left.\frac{\bar{\gamma}_U^2 - \bar{\gamma}_L^2}{2}\right|_2 = \left.\frac{\bar{\gamma}_U^2 - \bar{\gamma}_L^2}{2}\right|_1 \tag{2.35}$$

Since there is no loss of pressure head due to viscosity, the attachment point in the wake region will be a stagnation point with pressure coefficient of unity. The base pressure in the separation region must be adjusted to calculate base drag. Observation of actual 2-D flows shows that the base pressure is relatively constant throughout the separation bubble and is approximately that just outside of the separation streamline at the point of separation [43]. Thus the base pressure is taken here to be the mean of the pressures just upstream of the separation streamlines at the two separation points. It turns out that the pressures at these two points are nearly identical to one another.

2.2.5 Extension for Ground Effect Aerodynamics

The vortex panel method is extended here for the flow over a body in ground effect by using the method of images. An in-depth discussion of this method can be found in Ref. [48]. The method of images models a solid ground plane at $z = 0$ by placing the mirror image of the solid body at the negative value of the height. Due to symmetry across the $z = 0$ line, the no-penetration condition is automatically satisfied there. A schematic of the problem can be seen in Fig. 2.7. The subscript "1" refers to the image and the subscript "2" refers to the solid body. The method of images involves the analysis of flow over multiple bodies even if the original problem is for flow over a single solid body. For example, the flow over a single airfoil in ground effect is accomplished by analyzing the flow over two airfoils situated symmetrically about the intended ground plane (as is shown in Fig. 2.7). Since this flow involves two separation points (one at each trailing edge) and it is symmetric about $z = 0$, it automatically conserves vorticity in the entire region. It is very important to understand that vorticity conservation must be satisfied in each half region separately,

since the region of interest is just $z > 0$. Within the subregion, $z > 0$, vorticity conservation and shedding rates are determined identically to the out-of-ground effect counterpart.

There is no attempt made to satisfy a no-slip boundary condition on the ground plane. In the real flow problem, the ground plane would be moving at the free stream velocity as seen from a body-fixed coordinate system. This inability to match that boundary condition, along with the inviscid assumption causes a disparity in the predictions of this model with reality for the extreme ground effect case. For this case the flow between the vehicle and the ground plane is dominated by the diffusion of vorticity created at the two boundaries in close proximity to one another. The assumption of a thin viscous region (which we model with an infinity thin vortex sheet) breaks down since the viscous region will span the entire gap height between the vehicle and the ground plane when the flow becomes fully developed.

2.2.6 Flow Separation Model

Since the main flow solver is an inviscid one (no diffusion), important viscous effects need to be predicted by other means. Flow separation is the departure of the vorticity from the thin viscous region about the solid boundary into the flowfield. This occurs when the retarding effects of viscosity overcome the inertial forces of the fluid near the solid boundary. The location of separation along with the vorticity shedding rates at those points determines the circulation around the solid body and, therefore, the forces and moments. It is very important for the success of the optimization design to be able to consistently predict separation locations, at least relatively, from design to design.

The main separation region at the rear of the MAGLEV vehicle is definitely a turbulent separation due to the high cruise Reynolds number. The separation criterion used as part of this aerodynamic model is one developed by Stratford in 1959 [49]. This criterion is described by Eq. 2.36.

$$C_p \left(x \frac{dC_p}{dx} \right)^{\frac{1}{2}} \left(10^{-6} Re \right)^{-\frac{1}{10}} = \quad \text{Constant} \tag{2.36}$$

Stratford uses 0.39 for the constant if the curvature of the pressure distribution is positive and 0.35 if it is negative. It is obvious from this equation that the relation is only valid in regions of positive (adverse) pressure gradient. This equation is used in marching fashion from the point of minimum pressure to the point where the equation is satisfied (separation location). The Stratford criterion depends only upon values at the current location being evaluated making it simple to implement. The variable, x, is the distance along the surface measured from the point of minimum pressure. The pressure coefficient is measured relative to the pressure at the minimum pressure point. The Reynolds number is based on the surface velocity at the point of minimum pressure and a distance to a fictitious stagnation point. This distance is based on the momentum thickness of an equivalent turbulent flow over a flat plate. The value of the left hand side of Eq. 2.36 increases monotonically from its value of zero at the minimum pressure point to the value required for flow separation. It is clear from Eq. 2.36 that higher Reynolds numbers and lower adverse pressure gradients forestall the separation point.

Reference [50] discusses and compares several different separation criteria for incompressible, 2-D flow. The comparisons are based on performance in the prediction of separation location and pressure coefficient for a collection of experiments including both exterior and interior flows. The Stratford criterion is shown to consistently predict early separation. It was outperformed only by the modified Townsend criterion and the Boeing in-house boundary layer calculations. The superior performance came at the price of increased complexity. The modified Townsend criterion requires pressure coefficients upstream of the separation point and the skin friction coefficient at the point of minimum pressure. It also predicts a separation pressure coefficient rather than the actual separation location. The Boeing method requires an entire boundary layer calculation to be performed every time the separation location is to be updated. This would result in increased run times. The Stratford criterion was chosen for use here due to its easy implementation and consistent predictions. Figure 2.8 is a reproduction of a figure from Ref. [50]. It shows the predictions of the Stratford criterion compared with the experimental values of pressure coefficient at the separation point. The predictions are offset from the exact pressures although

the consistency can be seen in the banded nature of the predictions.

The location of separation is a function of several variables, one of which is the gradient of the pressure coefficient along the surface. Since the predicted velocity over the body surface is piecewise linear, the gradient of the pressure jumps discontinuously at the nodes between panels. This becomes a problem when the separation point moves from one panel to the next. The value of the Stratford criterion (the left hand side of Eq. 2.36) is therefore discontinuous at the nodes. In order to provide a continuously differentiable pressure distribution for the Stratford criterion, we replace the pressure distribution with piecewise cubic splines. A spline routine from Burden and Faires [51] is used to construct the clamped cubic splines using the pressure values at the nodes. This provides an analytic pressure distribution which is twice continuously differentiable over the whole surface. The Stratford criterion is satisfied using a bisection method which guarantees convergence to the separation location. A Newton or Secant method was not employed, since these methods run the risk of converging to the wrong root or diverging. The cubic splines are only used for the location of separation points. The calculated pressure coefficients are used for the integration of force and moment coefficients.

2.2.7 Solution to The Vortex Panel Method

The solution to the vortex panel method involves satisfying the no-penetration boundary condition over several time steps. At each time step, there are N unknowns representing the singularity strengths for the vortex sheet and $N + 1$ equations consisting of the no-penetration condition at the N collocation points and the statement of vorticity conservation. These equations can be seen for the discretized geometry in Appendix B. They are organized in the standard form of $Ax = b$.

The solution proceeds in the following fashion. After the geometry is read in, the panel lengths, collocation point locations, and time independent influence coefficients (the A matrix) are calculated. The time increment is calculated in order to have the free point vortices of the wake at a comparable distance to the nominal surface panel length. The number of time steps is chosen to allow a sufficient amount of time to

achieve a steady state. The vortex blob radius is calculated according to Eq. 2.30 which depends upon the calculated value of Δt.

Following the impulsive start, all calculations are made at every time step. The time dependent portion of the solution begins with the shedding of vortices from the previous time step according to Eq. 2.21 or Eq. 2.34. They are shed from the sharp trailing edge or the separation points for bluff body calculations. For the first time step, the vortices are shed from the second and n^{th} node and are of zero strength. The time dependent influence coefficients are calculated (the b vector). These consist of the wake influence coefficients, since a new vortex is shed after each time step and the position of all of the wake vortices changes during each time step. The current calculations do not involve any dynamic movement of the solid bodies, so the influence coefficients associated with the vortex sheet remain as part of the time independent matrix.

The system of linear equations is solved via a least squares optimization which minimizes the sum of the squares of the elements in the residual vector. This is done, since the system of equation is overdetermined by one equation. The DGELS subroutine from the LAPACK mathematics library is used for this calculation.

Once the no-penetration condition is satisfied for that time step, the locations of the shed vortices are updated according to the induced velocities and the separation location is updated according to the Stratford condition (for bluff bodies)(Eq. 2.36). At this point, we begin a new time step and shed vortices again. This set of calculations is repeated for the predetermined number of time steps. For the steady solution, the linear system of equations is solved once with the steady trailing edge condition as the auxiliary condition ($n + 1^{th}$ equation).

For simplicity sake, two different codes are used to calculate the flow for a sharp trailing edge body and a bluff body. These codes are named *pnlsharp* and *pnlbluff*. *Pnlbluff* can be seen in Appendix E. For the sharp trailing edge calculations, the pressure, force, and moment coefficients are calculated at the final time step when the flow is at steady state. The lift coefficient and drag coefficient are nondimensionalized by the chord, and the pitching moment coefficient is nondimensionalized by the chord

squared (Eq. 2.37).

$$\begin{aligned} C_L &= \frac{L}{qc} \\ C_D &= \frac{D}{qc} \\ C_m &= \frac{m}{qc^2} \end{aligned} \tag{2.37}$$

Since the bluff body flow never truly becomes steady, the coefficients are averaged over several time steps after the circulation becomes steady in the mean. The lift coefficient and drag coefficient are nondimensionalized by the maximum thickness (d) and the pitching moment coefficient is nondimensionalized by the thickness and chord (Eq. 2.38).

$$\begin{aligned} C_L &= \frac{L}{qd} \\ C_D &= \frac{D}{qd} \\ C_m &= \frac{m}{qdc} \end{aligned} \tag{2.38}$$

2.2.8 Skin Friction Model for Out-of-Ground Effect Case

The skin friction drag calculation is performed using the PMARC_12 boundary layer analysis which includes the Thwaites/Curle integral method for the laminar boundary layer and the Nash/Hicks integral method for the turbulent boundary layer calculations. A detailed description of the boundary layer analysis can be found in the PMARC_12 operating manual [52]. Empirical relations are used to determine laminar separation with turbulent reattachment and natural transition. Turbulent separation occurs when the friction velocity goes to zero. The implementation of this portion of PMARC_12 involves the proper connection of the 2-D vortex panel method flow solver with the PMARC_12 boundary layer calculation subroutines as a post processor. The viscous flow analysis is performed only once for each geometry following the completion of the time stepping inviscid flow solution.

2.2.9 Skin Friction Model for Ground Effect Case

For the ground effect case, the viscous flow in the gap between the vehicle and the guideway is modeled using a turbulent Couette/Poiseuille flow calculation in a 2-D channel. The flow in the non-parallel sections of the train underbody is ignored for simplicity. The flow is assumed to be fully developed over the whole length, and the single skin friction coefficient obtained from this calculation is applied over every panel on the vehicle underbody. The turbulent Couette/Poiseuille flow can be determined by solving Eq. 2.39. This equation can be solved by numerical integration. A detailed outline of the solution procedure can be seen in Appendix C along with a schematic diagram of the flow.

$$\begin{aligned} \frac{dp}{dx} &= \frac{d}{dy}\left[(\mu+\mu_T)\frac{du}{dy}\right] \\ u_0 &= 0.0 \\ u_h &= u_\infty \end{aligned} \tag{2.39}$$

The eddy viscosity is modeled separately in the inner and outer regions. Since it was found that the Law of the Wall also applies to pipe flows, the Reichart turbulence model is used for the inner region (Eq. 2.40).

$$\mu_T = k\rho\nu\left[\left(\frac{yu_*}{\nu}\right) - y_a^+ \tanh\left(\frac{yu_*}{\nu y_a^+}\right)\right] \tag{2.40}$$

For the outer region, the eddy viscosity is calculated using a model for internal flows suggested by Reynolds [53].

$$\mu_T = 0.192k\rho u_* h \tag{2.41}$$

These turbulence models require the calculation of the friction velocity, u_*, which depends upon the wall shear stress. The integration of Eq. 2.39 is therefore embedded within a root finding scheme for the wall shear stress. The pressure gradient is a constant and is determined by the vortex method solution of the inviscid flowfield. The subroutine which performs this calculation can be seen in Appendix E.

The results of this viscous flow analysis are compared with experimental values obtained by El Telbany [54]. These experiments were for fully developed turbulent

flow between parallel walls with one wall moving. This was accomplished using a moving belt in a wind tunnel. Measurements were made for many cases of varying wall separation, wall velocity, and mass flow. Plots for three different mass flows can be seen in Fig. 2.9. This plot shows two solutions for Couette type flows which are flows in which the ratio of wall shear stress is positive and a solution for Poiseuille type flows which are flows in which the ratio of wall shear stress is negative. There is excellent agreement between the calculated velocity profiles and the experimental velocity profiles. The mass flow was determined by numerically integrating the velocity data points.

2.2.10 Verification of the 2-D Model

This subsection was written with two purposes in mind. The first is to show the differences between the doublet panel method and the vortex panel method, especially when dealing with ground effects flows. Calculations were performed on a Clark Y airfoil for this purpose. The second purpose is to examine several flows using the vortex panel method to verify it for use in the optimization loop. Bluff body flows were calculated for a circular cylinder and a 3.5:1 elliptic cylinder. Calculations were then made for the side view of the Northrop Grumman MAG950 and MAG1002 designs.

The Clark Y airfoil was chosen for the purpose of comparing the doublet panel method and the vortex panel method due to its flat underside. This will allow us to see the main difference between these two methods. The Clark Y is situated at an angle of attack of approximately 2^o such that the flat underside is perfectly horizontal. The airfoil at angle of attack and surface grid can be seen in Fig. 2.10. Since this is a sharp trailing edge flow, the flowfield can be solved in either a steady or unsteady fashion. The unsteady calculation is an impulsively-started problem. A wake is shed over successive time steps until the flow reaches steady state.

A plot of vortex panel method pressure coefficient for the Clark Y out-of-ground effect can be seen in Fig. 2.11 for a steady calculation, as well as for an unsteady calculation with 400 time steps and one unsteady calculation with 800 time steps.

This plot shows that as the unsteady solution is allowed to progress in time the solution approaches that of the steady flow. The 2-D flow over a sharp trailing edge body requires many time steps to reach steady state, since the starting vortex must move a sufficient distance from the airfoil (which is infinite in span). A rule of thumb is that the wake should be allowed to develop to approximately 30 chords in length. Since we are only concerned here with bodies in translation all of the remaining calculations for sharp trailing edge flows are performed in a steady fashion.

Figure 2.12 shows a comparison of the pressure coefficient over the Clark Y airfoil out-of-ground effect calculated by the doublet panel method and the vortex panel method. This plot shows general agreement in the predicted pressure coefficient with some slight difference on the lower surface and at the trailing edge. These small differences can be attributed to the difference between discrete and continuous surface singularities as well as the different (yet consistent) implementation of the trailing edge conditions.

Figure 2.13 shows a comparison of the pressure coefficient over the Clark Y airfoil in ground effect calculated by the doublet panel method and the vortex panel method. The airfoil is situated at an altitude of $1/10^{th}$ chord. There is a large difference in the pressure coefficient calculated by these two methods. An interesting and enlightening result is the difference in the pressure coefficient predicted for the lower surface. This lower surface is in close proximity to the ground plane, and the flow between these two surfaces is essentially a 2-D flow in a narrow gap. The doublet panel method predicts a uniform pressure along this gap which is the expected result of a linear method. On the other hand, the vortex panel method predicts a pressure drop in the gap in qualitative agreement with real flows. This result is usually attributed only to high-order aerodynamics methods and is predicted here due to the better kinematic match between the vortex panel method and a real flow.

Figure 2.14 is a plot of the Clark Y lift coefficient as a function of the height-to-chord ratio. Since the airfoil has a flat bottom, there is only a slight loss of lift prior to lift reversal ($\Delta C_L = -0.0040$). Lift reversal is evident as the height-to-chord ratio approaches zero. Figure 2.14 also shows points for the doublet panel method predictions for out-of-ground effect and $0.1c$ in ground effect flows. As was the case

for the pressure coefficient profiles, the out-of-ground effect predictions are similar for these two methods, while the ground effect predictions show a large difference. The doublet panel method predicts only a slight increase in lift due to the close ground proximity. The effect of height-to-chord ratio on pitching moment about the leading edge can be seen in Fig. 2.15. Pitching moment also reverses from a slight increase to a large negative change as height-to-chord ratio approaches zero. The remainder of the calculations in this work employ the vortex panel method due to its superior performance for ground effect predictions.

The vortex panel method for 2-D bluff body flow was verified on several infinite cylinders, the first of which is the circular cylinder. The initial calculations were performed with the vortex panel method and no flow separation model. Figure 2.16 shows the surface pressure coefficient over the circular cylinder for both the out-of-ground effect and ground effect cases. The out-of-ground effect case shows excellent agreement with the analytic solution for potential flow over a circular cylinder (Eq. 2.42).

$$C_p = 1 - 4\sin^2\theta \tag{2.42}$$

The angle θ in this equation is the polar coordinate. Negative lift is predicted for the ground effect flow due to accelerated potential flow under the cylinder. This negative lift becomes greater as the height-to-diameter ratio decreases. Lift reversal cannot be predicted at this level, since the mechanism for this phenomena is in the location and strength of vortex shedding. Figure 2.17 shows the velocity profile along the vertical centerline of the circular cylinder for the out-of-ground effect case. Along this line, the only component of the velocity is in the horizontal direction. The velocity profile matches the analytic solution, which can be seen in Eq. 2.43.

$$\frac{u}{U_\infty} = \cos\theta\left(1 - \frac{R^2}{r^2}\right) + \sin\theta\left(1 + \frac{R^2}{r^2}\right) \tag{2.43}$$

R is the radius of the circular cylinder. Figure 2.18 shows the velocity profile along the lower vertical centerline of the circular cylinder for the ground effect case. This plot shows the nature of the image method velocity profile which is neither a true road condition nor a wind tunnel condition. The wind tunnel condition is characterized by

a ground plane velocity of zero while the road condition is characterized by a ground plane velocity equal to the free stream velocity.

Calculations were next performed on the circular cylinder using the vortex panel method with the bluff body separation model. These calculations were performed at a Reynolds number of 8.6 million. For the bluff body calculations, Reynolds number is used to determine the skin friction drag and the separation location, while for sharp trailing edge bodies, Reynolds number only enters the problem in the skin friction drag calculation. The vortex panel method itself is still an infinite Reynolds number calculation. The flow developed for 0.5 seconds which was sufficient to reach steady state. A vortex blob diameter of $3.5V_\infty\Delta t$ is required to obtain a stable solution. Figure 2.19 shows the pressure coefficient for the out of ground effect case as compared to experimentally obtained values [55]. The pressure coefficients shown here are the mean values over the last eighty time steps, since the solution is always unsteady. This plot shows that as Reynolds number increases the pressure coefficient plots are approaching that for the infinite Reynolds number limit vortex method prediction. The base pressure decreases with increased Reynolds number, while the surface pressures prior to separation increase. This difference prior to separation can be accounted for by the displacement thickness of the boundary layers for the finite Reynolds number cases.

Figure 2.20 shows the calculated shed vortex sheets which roll up into the Von Karman vortex street. Separation occurs at approximately 105^o where 0^o is the most upstream point. A time history of the lift and drag coefficients for the out-of-ground effect calculation can be seen in Fig. 2.21. Lift and drag coefficient are based on cylinder diameter. The calculation takes around 50 time steps to settle out from the impulsive start after which the flow exhibits oscillating behavior. We obtained a Strouhal number of 0.359 and a mean drag coefficient of 0.8371 based on cylinder diameter. Both of these numbers compare favorably with published experimental values shown in Delany [56] and Roshko [57]. The drag coefficient is slightly high due to the lower base pressure of the infinite Reynolds number limiting case. The Strouhal number is also higher than the Roshko data at Reynolds numbers ranging from 4 to 8 million (0.26 to 0.28). Delany measured Strouhal numbers ranging between 0.3 and

0.4 at slightly lower Reynolds numbers (1 to 2 million).

Ground effect calculations were performed on the circular cylinder for comparison with experimental data both published (Bearman and Zdravkovich [58]) and obtained in house. Bearman and Zdravkovich performed wind tunnel experiments on a circular cylinder over a fixed ground plane. They tested at a Reynolds number of 48000 based on cylinder diameter and used a trip strip to obtain turbulent flow over the ground plane. This Reynolds number is clearly subcritical for flow over a circular cylinder. Subcritical flow involves laminar separation while supercritical flow involves turbulent separation. Experiments were also performed at Virginia Tech in the open jet wind tunnel which has a 0.99 meter diameter test section exit. The experiments were performed for two of Bearman's ground clearances at a higher Reynolds number (300000) although it was still too low to provide supercritical flow. This tunnel can provide supercritical flow at a Reynolds number of 250000 for out-of-ground effect flows due to the tunnels high free stream turbulence (approximately 4%). Figures 2.22 through 2.25 show the pressure coefficients over the circular cylinder for the different experiments and the vortex panel method calculations. These figures show the results at height-to-diameter ratios of 0.1, 0.4, 1.0, and 2.0 respectively. The Virginia Tech experiments (indicated by the author's last name) were performed for the two lowest ground clearances. These experimental results match those of Bearman. The vortex panel method which only predicts supercritical flow naturally differs from the experimental results. The delayed separation which is characteristic of supercritical flow results in the greater acceleration of the flow as it remains attached until after the maximum thickness of the cylinder.

Calculations were also performed on a 3.5:1 elliptic cylinder in order to compare the vortex panel method results to the RANS calculations and experiments of Ranzenbach and Barlow [59]. These were performed at a Reynolds number of 1.5 million based on chord. Force and moment coefficients are also based on the chord (length of the major axis). The RANS calculations were performed for both wind tunnel conditions ($u(y = 0) = 0$) and road conditions ($u(y = 0) = V_\infty$) while the vortex method uses the method of images. The experiments were performed for wind tunnel conditions only. Figure 2.26 shows the elliptic cylinder and its surface grid for

the vortex panel method. The vortex panel method was solved over three seconds which was sufficient to reach steady state flow. A vortex blob diameter of $5V_\infty \Delta t$ was required to obtain a stable solution. For the out-of-ground effect case, the vortex panel method predicted a drag coefficient of 0.0465 compared to the RANS prediction of 0.0394. Figure 2.27 shows the lift coefficient as a function of the height which is nondimensionalized using the length of the minor axis of the ellipse. Figure 2.28 shows the drag coefficient as a function of the height ratio. As the height is decreased, both the predicted lift coefficient and the drag coefficient increase. They also have higher values than the experimental values or the RANS calculations. The general trends of the coefficients as a function of the nondimensional height are captured by the vortex panel method as well as reasonable numerical values.

Some insight into these results can be gained by looking at the separation and stagnation point locations. Figure 2.29 shows the separation locations and stagnation point locations for the elliptic cylinder out-of-ground effect. The vortex panel method using Stratford's criterion predicted separation aft of the RANS predictions. The vortex panel method predicted a higher out-of-ground effect drag coefficient due to a lower base pressure coefficient prediction. Figures 2.30 and 2.31 show the same information for the ground effect case at nondimensional altitudes of 0.473 and 0.175 respectively. The vortex panel method predicts greater augmentation of the separation locations and stagnation point locations resulting in greater lift reversal as the ground clearance is decreased.

Lastly, calculations were performed to verify the vortex panel method against Northrop Grumman RANS calculations [28] for the flow over a 2-D MAGLEV vehicle in ground effect. The RANS calculations were performed to match wind tunnel conditions for experiments performed by Tyll, Liu, and co-workers [8] [60] at Virginia Tech. These were for a $1/10^{th}$ scale model at a Reynolds number of 3.75 million per meter. The scaled vehicle studied here is $2.4m$ in length and cruises at an altitude of $0.01m$. The vortex blob diameter is set at $1.75V_\infty \Delta t$ for the ground effect case to obtain stable solutions. Figure 2.32 shows the paneling for the Grumman MAG950. Figure 2.33 shows the vortex sheets calculated for the Grumman MAG950 design for both in and out-of-ground effect. The out-of-ground effect (OGE) calculation shows

the development of the Von Karman vortex street. The starting vortex is evident at the downstream end of the sheet. This flow structure is disrupted by the presense of the ground plane for the in ground effect (IGE) case.

Figure 2.34 shows a plot of pressure coefficient versus the nondimensional vehicle length for the Northrop Grumman MAG950. This plot shows excellent agreement between the RANS calculation and the vortex method calculation. The vortex panel method predicts a reasonable pressure drop of the gap flow as well as a reasonable base pressure (slightly high). The difference in the pressure coefficient at the aft end of the vehicle is due to the buildup of a boundary layer for the RANS case. The increasing boundary layer thickness provides for a more moderate adverse pressure gradient over the top surface. The thick viscous region on the lower surface accounts for the difference in pressure coefficient on that surface at the aft end of the vehicle. The vortex panel method solution shows an expansion as the flow leaves the parallel section of the underbody just prior to the section of attempted pressure recovery. Figure 2.35 shows a plot of pressure coefficient versus the nondimensional vehicle length for the Northrop Grumman MAG1002. It too shows an excellent match of the vortex panel method solution to the high-order, RANS calculations. The pressure drop in the gap is predicted well along with an excellent match for the base pressure.

The integrated force and moment coefficients calculated by the vortex panel method are shown for the five 2-D, Northrop Grumman designs in Table 2.1. These coefficients are based upon the vehicle height, and the pitching moment coefficient is taken about the leading edge of the vehicle. These values show similar qualitative results to the RANS calculations performed by Northrop Grumman. The highest drag coefficients are experienced by the MAG950 and MAG1007 designs. The major difference in the predictions is for that of the MAG1459 which we predict to have an extremely low drag coefficient as compared to the other designs. The prediction of such a low drag is due to a high leading edge suction which will be explained in the results sections. The optimum drag coefficient designs have a similar shape to the MAG1459. The drag breakdown for these vehicles shows that all of these side view shapes yield between 70% and 75% of the total drag due to base drag. Since a majority of the skin friction drag is due to the viscous flow in the gap between

the track and vehicle, attempts to lower the drag coefficient will deal mostly with a reduction in base drag. So, potential drag coefficient improvement via changes in the vehicle shape is around 75%.

Tables 2.2 and 2.3 show the lift and drag coefficient comparisons between in and out-of-ground effect flow for the MAG950. These comparisons are done here for the wind tunnel scale case. Lift reversal is evident as the lift coefficient increases by approximately 180% of its out-of-ground effect value for the altitude of 0.01 meters ($\frac{h}{d} = 0.029$). The drag coefficient for the IGE case is higher than the OGE case due to increases in both skin friction drag and base drag. The table shows that the base drag makes up approximately 64% of the drag increase. The out-of-ground effect values closely match those predicted by the RANS calculations [28]. They predicted a lift coefficient of around 1.0 and a drag coefficient of around 0.16. Similar to the Northrop Grumman study, the vortex panel method predicted an approximate doubling of the drag coefficient when the vehicle is brought in ground effect.

The verification for flow over the MAGLEV vehicles was performed at wind tunnel scale, although, all of the design optimizations are performed at full scale conditions. A comparison of wind tunnel to full scale condition calculations can be seen in Fig. 2.36 and 2.37. Figure 2.36 shows the pressure coefficient over the Northrop Grumman MAG950 out-of-ground effect as calculated by the vortex method. The two cases are for the full-scale Reynolds number of 30.0 million and the wind tunnel case with Reynolds number of 1.3 million. The pressure coefficient predictions show nearly identical profiles except for the aft end of the vehicles. The difference between these two profiles is caused by the later separation for the full scale case due to the higher Reynolds number. In addition to this, force and moment coefficients differ, since no attempt was made to fix the location of the boundary layer transition. For the MAG950, out-of-ground effect, the lift coefficient for the wind tunnel scaled case is 1.2024 and that for the full scale vehicle is 1.4130. The drag coefficient for the wind tunnel case is 0.168 and that for the full scale case is 0.147. These can be seen in Table 2.4.

Figure 2.37 shows the pressure coefficient over the Northrop Grumman MAG950 in ground effect as calculated by the vortex panel method. The two Reynolds number

cases are shown. The profiles for the ground effect case show similar results to that of the out-of-ground effect case. The pressure coefficient profiles are nearly identical over most of the vehicle surface. The full-scale case experiences a later separation than the wind tunnel scale case, since the Reynolds number is higher. It, therefore, expands more prior to the attempted pressure recovery and recovers to a higher pressure coefficient than the wind tunnel scale case. The drag coefficient for the full scale case is lower than that for the wind tunnel scale case (0.203 and 0.253 for the MAG950 full scale and wind tunnel scale respectively). The lift coefficient is higher for the full scale (3.461) than for the wind tunnel scale (3.362) for the MAG950. These numbers can be seen in Table 2.5.

The test cases for the 2-D aerodynamics model shows that the 2-D, ground effect flow around bluff bodies can be consistently modeled using the vortex panel method. Lift reversal is captured with the use of the Stratford criteria for determining the separation locations and the proper modeling of the mechanics of viscous flow. Differences between the vortex panel method predictions and the accepted true values are accounted for by the vortex panel method assumptions, in particular the infinite Reynolds number limit and the implementation of the ground effect using the method of images. The results are qualitatively consistent and quantitatively realistic. The 2-D vortex panel method makes an excellent analysis tool for integration in an MDO design methodology due to its performance and quick calculation times (approximately 6.5 CPU minutes for a 104 panel MAGLEV side view design on a Silicon Graphics Power Challenge with an R8000 processor chip).

2.3 3-D Model

This section considers the two different models which are 3-D extensions to the 2-D doublet panel and vortex panel methods. The 3-D doublet panel method used here is PMARC_12 (Panel Method Ames Research Center) [52]. The 3-D extension to the vortex panel method was developed by Mracek and Mook [40] [61]. The doublet panel method is equipped with an image method ground plane simulation. It was extended for flow around a bluff body. The vortex panel method has an unsteady wake

model which can be used for a closed tube wake. The code available to us, which was written by Mracek, is formulated specifically for thin lifting surfaces. An extension for thick lifting bodies is unavailable. This code is extended for ground effect flow via the image method. Since there are no 3-D turbulent separation criteria, we only consider geometries with known separation locations. Each model is discussed in its own subsection below. The work presented here does not include the integration of these 3-D aerodynamics models into the MDO framework. The intention here is to evaluate their capabilities with respect to such an integration.

2.3.1 3-D Doublet Panel Method

The 3-D doublet panel method implementation used here is PMARC_12. This code involves the solution to Laplace's equation based on Green's Identity. A discussion of Green's Identity and its application to the solution to Laplace's equation in 3-D can be seen in Appendix D. A more detailed discussion can be seen in the PMARC_12 manual [52]. This method employs a 3-D source distribution and a 3-D doublet distribution. The source strength is set to cancel out the normal component of the free stream flow. This results from the mathematical statement of no penetration and the implicit formulation (Dirichlet) of that boundary condition. The 3-D distributed doublet singularity is mathematically identical to a ring vortex on the panel perimeter. So, like its 2-D counterpart, PMARC_12 deals with discrete vorticity which is kinematically different from a real fluid flow over a solid surface.

The auxiliary condition for a trailing edge used in PMARC_12 is the steady state implementation of the Kutta condition (Eq. 2.7). This condition is used in PMARC_12 for both steady and unsteady flow. This wake model is incorrect and has been changed here to that which is shown in Eq. 2.8. This wake model is for an unsteady flow and will converge to steady state conditions if the solution is permitted to sufficiently develop in time. It can also be used for the flow over a bluff body with separation (closed tube wake) according to the assumptions discussed in Section 2.2.4 for 2-D flow. Ground effect is simulated using the method of images.

2.3.2 Verification of 3-D Doublet Panel Method

The 3-D doublet panel method, PMARC_12, was verified first for the flow over sharp trailing edge bodies and bluff bodies. We also looked at the prediction capabilities of ground effect flow. The verification was also performed to look at the corrected separation line condition which employs the unsteady implementation of the Kutta condition.

To verify the prediction capability for the flow over a sharp trailing edge body, we used an aspect ratio 1.0 rectangular wing with a ClarkY airfoil section. The wing is situated at an angle of attack, so that the flat underside is aligned with the horizontal. Flow calculations are performed using both the steady trailing edge condition (which comes with PMARC) and the unsteady trailing edge condition (which was written into the code by the author). A time history of the lift coefficient for the impulsively started wing can be seen in Fig. 2.38. The top plot is for out-of-ground effect flow and the bottom plot is for ground effect flow. The solutions via the two different trailing edge conditions appear to arrive at approximately the same steady state lift coefficient although the unsteady trailing edge formulation predicts a longer transient. The out-of-ground effect lift coefficient is approximately 0.16 while the ground effect lift coefficient is approximately 0.18 (based on planform area). The wing and the shed vortex sheet can be seen in Fig. 2.39 for the out-of-ground effect case and in Fig. 2.40 for the ground effect case. The wake for the ground effect case spreads out laterally due to the induced velocity of the image wake. This is in agreement with the observed behavior of wing tip vortices near the ground. If one's interests are only in the steady state coefficient values, then the original PMARC wake model can suffice. However, the unsteady model can provide time accurate values for the flow over a sharp trailing edge body and is essential for the flow over a bluff body.

Bluff body flow was verified using a sphere, since there is an abundance of data to compare against and the separation location is widely known. Since the flow over a bluff body is never truly steady, the unsteady wake model was used. The use of the steady trailing edge conditions for the case of a bluff body with a closed tube wake would force a closed stagnation line which is not physically possible. A solution time history for the impulsive start of flow over a sphere can be seen in Fig. 2.41. Flow is

set to separate at approximately 104°, according to the accepted value for turbulent flow over a sphere. The drag coefficient becomes steady after approximately 11 time steps. Figure 2.42 shows the pressure coefficient predicted by PMARC as compared to experimentally determined values at a Reynolds number of over 4×10^5 [62]. There is excellent agreement between the doublet panel method and the experimentally determined values. Figure 2.42 also shows a portion of the shed closed tube vortex sheet behind the sphere.

2.3.3 3-D Vortex Panel Method

The 3-D vortex panel method is a 3-D version of the 2-D vortex panel method and was developed by Mracek and Mook [40] [61]. It is an alternative to the vortex lattice method which has discrete panels with concentrated vorticity (equivalent to the doublet panel method). In this model, the solid surface of a body is modeled using a continuous vortex sheet which represents the thin viscous region much the same as was done for the 2-D vortex panel method. The sheet strength is set up to vary linearly along the sides of the elements by using hat functions. These elements (panels) are triangular so that all of the vertices lie on the surface of the body. Such panels provide smoothly varying values of pressure and velocity. The layout of the elements can be seen in Fig. 2.43.

The calculation of the flow over lifting bodies is handled by shedding a wake which develops over time. The kutta condition is implemented in a similar fashion as was done for the 2-D vortex panel method. This implementation employs Euler's (or Bernoulli's) equation, and the Kutta condition is imposed in the most general sense which is for unsteady conditions. This condition will reach a steady state if the wake is permitted to shed for a sufficient number of time steps. Based on the same assumptions as were made for the 2-D case, one can also use this condition for bluff body flow (closed tube wake). If we ignore entrainment, we can treat a separation bubble by simply stating that the pressure on either side of the shed wake near the separation point is identical. Using this trailing edge condition (described in detail for the 2-D case) it is apparent that the vorticity from the infinitely thin viscous

region is shed into the wake. The wake is still modeled using discrete vorticity (ring vortices) identical to those is the doublet panel method. A vortex edge core lies along the trailing edge or the separation line (for the bluff body case) in order to attach this discrete vorticity wake to the continuous vortex sheet. This is required in order to have nonzero vorticity at such a separation line. The strength is chosen so that the gradient of the circulation around the core in the direction parallel to the line of separation is equal to the negative of the sheet strength at that point. The piecewise linear sheet strength will, therefore, result in a quadratic circulation distribution. The strength of the adjoining vortex ring is the mean value of the circulation along that segment of the edge core (Fig. 2.43). Spatial conservation of vorticity in the wake is maintained by using an adaptive mesh to split rings into smaller ones when they stretch out too much.

This method is a linear one which involves the solution to Laplace's equation via the linear superposition of analytic solutions to the equation. These analytic solutions are the vortex sheet which models the thin viscous region near the solid surface, ring vortices which are used to model the convected wake, and the edge cores used to join them. The strengths of all of the elements are determined in order to satisfy the no-penetration boundary condition on the surface. This is shown here as a system of linear equations

$$\begin{aligned} \mathbf{V}\cdot\mathbf{n} &= 0 \\ \left[\begin{array}{cc} A+C & D \end{array}\right]\left\{\begin{array}{c} \mathbf{\Omega} \\ G \end{array}\right\} &= \{U-W\} \end{aligned} \tag{2.44}$$

where $\mathbf{\Omega}$ is the vorticity and G is the strength of the discrete wake elements, U is the free stream velocity, and W is the velocity induced by the wake elements shed at previous time steps.

In order for the vortex sheet to resemble a viscous fluid region near a solid surface, the vorticity field must be solenoidal. This is due to the vorticity being the curl of the velocity vector field. The divergence of the curl of any vector field must be zero. For the 2-D vortex panel method this was satisfied automatically, since the vorticity and velocity vectors are always perpendicular to one another. For 3-D flow, this is

not the case, so the divergenceless condition must be satisfied explicitly.

$$\begin{aligned} \nabla \cdot \gamma &= 0 \\ \begin{bmatrix} B & 0 \end{bmatrix} \begin{Bmatrix} \mathbf{\Omega} \\ G \end{Bmatrix} &= \{0\} \end{aligned} \tag{2.45}$$

The compatibility condition at the separation lines is shown below.

$$\begin{aligned} \frac{d\Gamma}{dx} &= -\gamma \\ \begin{bmatrix} E & F \\ J & 0 \end{bmatrix} \begin{Bmatrix} \mathbf{\Omega} \\ G \end{Bmatrix} &= \{0\} \end{aligned} \tag{2.46}$$

As was already mentioned, the Kutta condition is implemented using Bernoulli's equation and setting the pressures across the separation line (or trailing edge) equal to one another.

$$\begin{aligned} \Delta C_p &= 0 \\ \begin{bmatrix} K & L \end{bmatrix} \begin{Bmatrix} \mathbf{\Omega} \\ G \end{Bmatrix} &= \{P\} \end{aligned} \tag{2.47}$$

Instead of working through the algebra to obtain a square system of equations, the problem is solved using a least squares optimization to minimize the sum of the squares of the residual. The divergenceless condition, compatibility condition, and Kutta condition are treated as weighted constraints. This complete system of equations can be seen in Eq. 2.48.

$$\begin{bmatrix} A+B & D \\ w_1 B & 0 \\ w_2 E & w_2 F \\ w_3 J & 0 \\ w_4 K & w_4 L \end{bmatrix} \begin{Bmatrix} \mathbf{\Omega} \\ G \end{Bmatrix} = \begin{Bmatrix} U - W \\ 0 \\ 0 \\ w_4 P \end{Bmatrix}. \tag{2.48}$$

Just as for the 2-D vortex panel method, the 3-D version solves directly for the surface velocity if we impose the no-slip condition at the solid surface. The strength of the vortex sheet (vorticity) is equal in magnitude to the boundary layer edge velocity

but is rotated 90° about an axis normal to the surface at that point. The specifics associated with this method and the matrix elements are covered in the previously cited work by Mracek and Mook. This method provides a better kinematic match to a real, high Reynolds number, viscous flow than the doublet panel method.

Ground effect is implemented using the method of images. It is only necessary to augment Eq. 2.44 with the influence coefficients for the image of the body, edge core, and wake. The divergenceless condition only needs to be satisfied in the real region. That is also the case for the compatibility condition and the kutta condition.

The code written by Mracek, *threed.f*, is set up for two specific types of flows; non-lifting flows over thick bodies, and lifting flows over thin bodies. An attempt was made to extend Mracek's code for lifting flow over thick bodies although the reformulation was never successful. Calculations were made for lifting flow over thin bodies for both the out of ground effect and in ground effect cases. An extension of this design methodology for full 3-D designs should consider the development of such a model.

2.3.4 Verification of 3-D Vortex Panel Method

The 3-D vortex panel method was used to calculate the flow over a rectangular wing with aspect ratio 1.0 and a Clark Y airfoil section in an attempt to draw a comparison to the 3-D doublet panel method, as was done for the 2-D case. This computation is for a thin body so a mean camber line for the Clark Y is used. The lift coefficient for the out-of-ground effect case is 0.125, based on planform area. The wing and the shed wake can be seen in Fig. 2.44. The lift coefficient for the ground effect case in 0.084. Lift reversal is not predicted. The wing and the shed wake for the ground effect case can be seen in Fig. 2.45. One cannot draw a comparison between the discrete vorticity, doublet panel method, and the continuous vorticity, vortex panel method for 3-D ground effect flow while using this thin body formulation. A general discussion of the vortex panel method for thick lifting bodies can be found in Ref. [61].

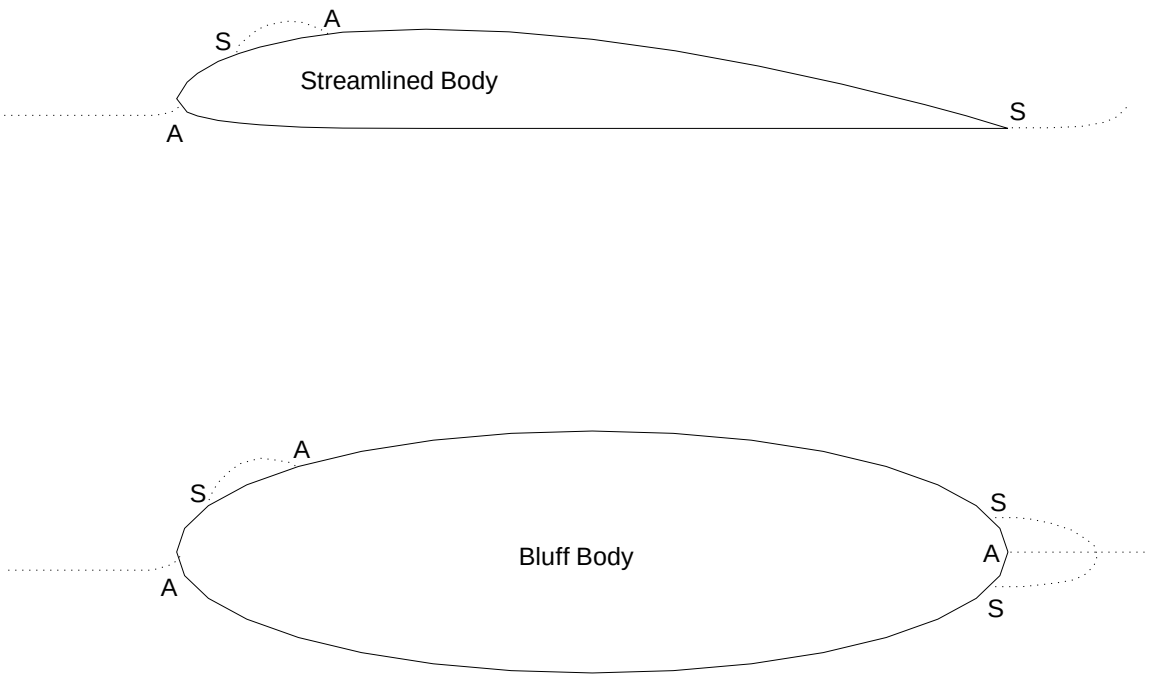

Figure 2.1: Attachment (A) and Separation (S) for Different Flow Situations (after Ref. [46])

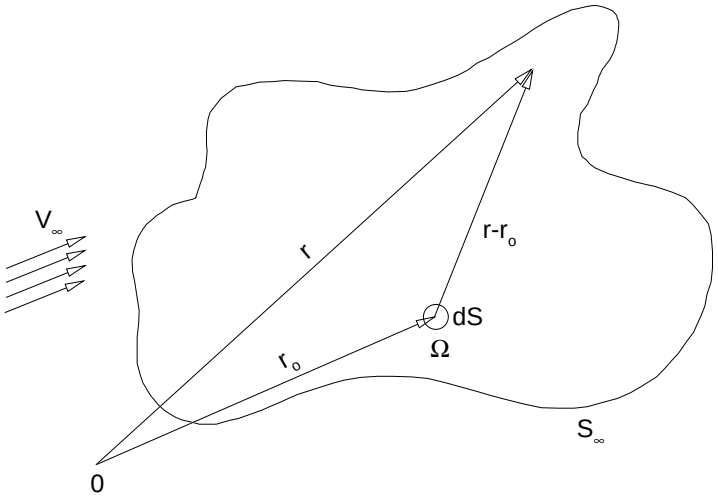

Figure 2.2: Schematic of Biot-Savart Law

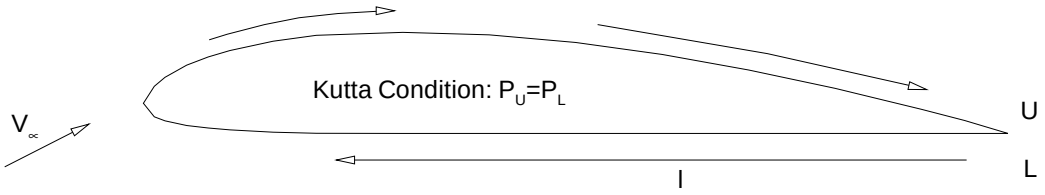

Figure 2.3: Path of Integration of Euler's Equation Around Airfoil

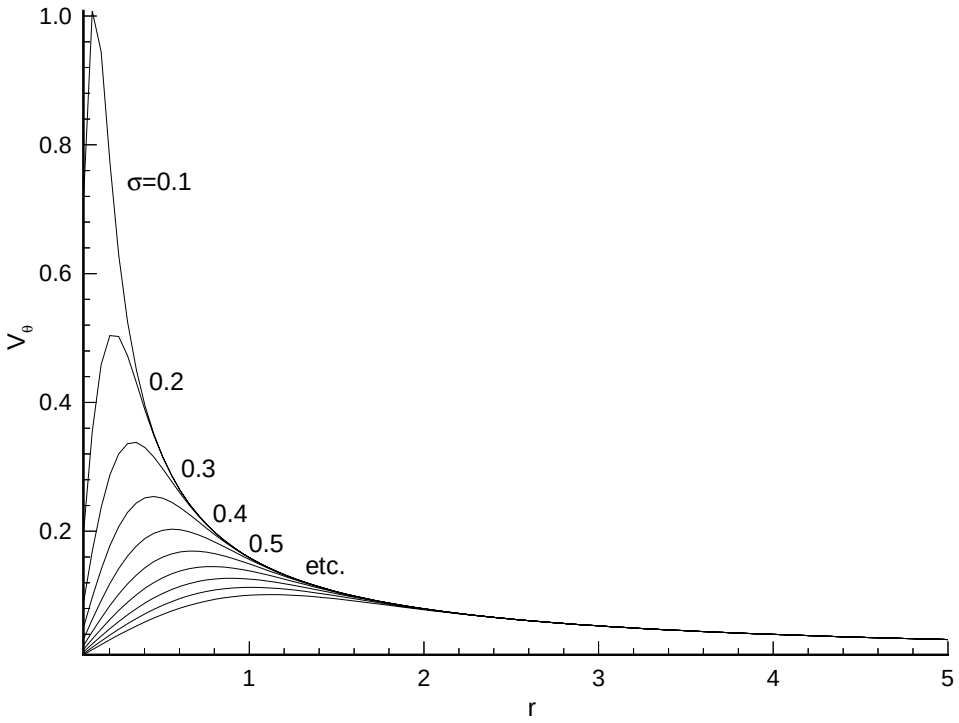

Figure 2.4: Gaussian Core Distribution for Vortex Blob Method

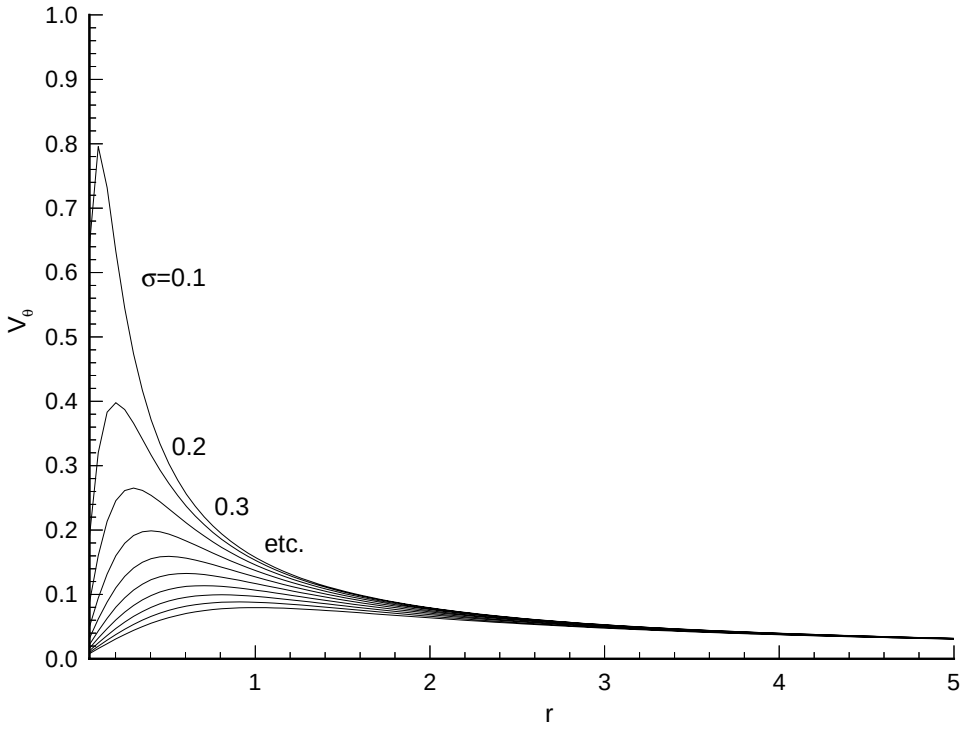

Figure 2.5: Vortex Blob Method Distribution Function

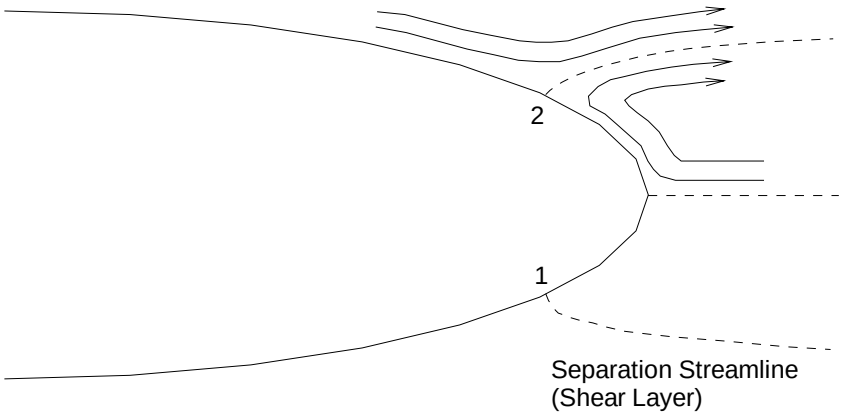

Figure 2.6: Two Dimensional Flow Separation

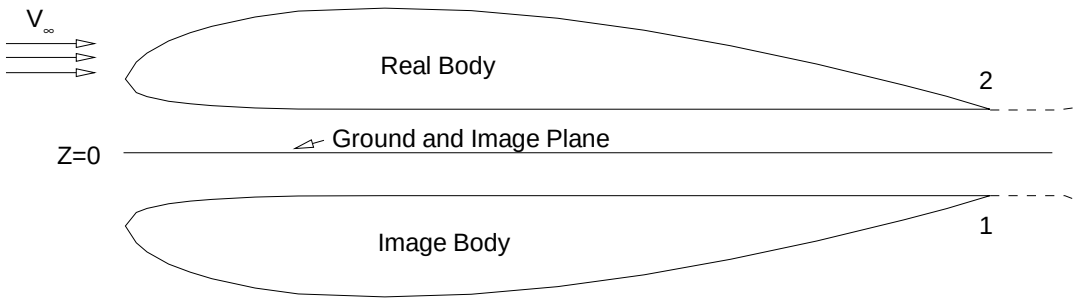

Figure 2.7: Schematic of Method of Images

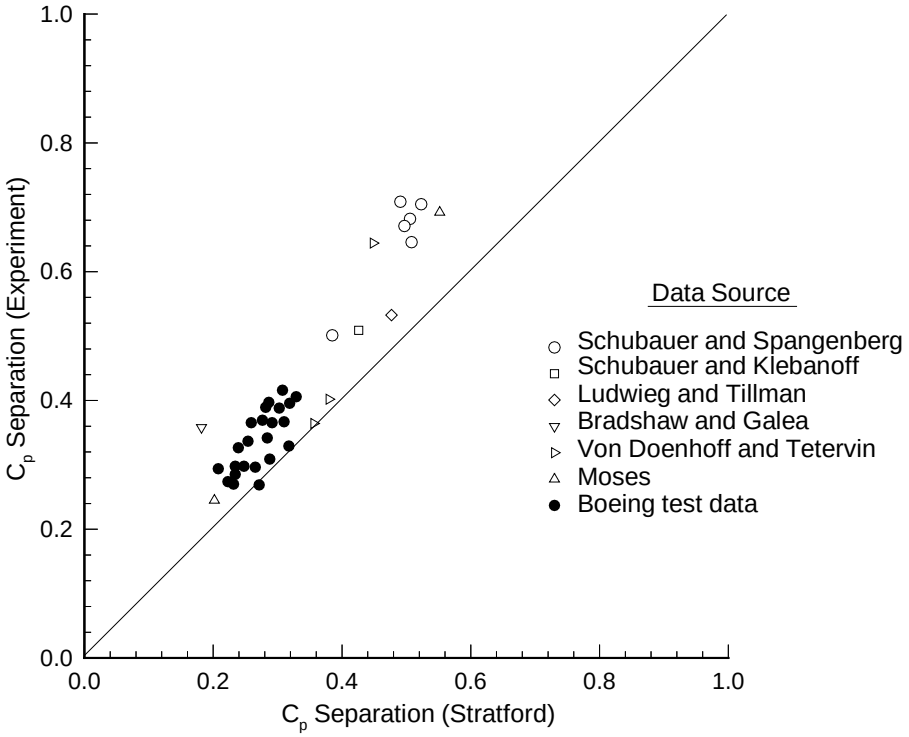

Figure 2.8: Evaluation of Stratford's Separation Criterion with Experimental Data [50]

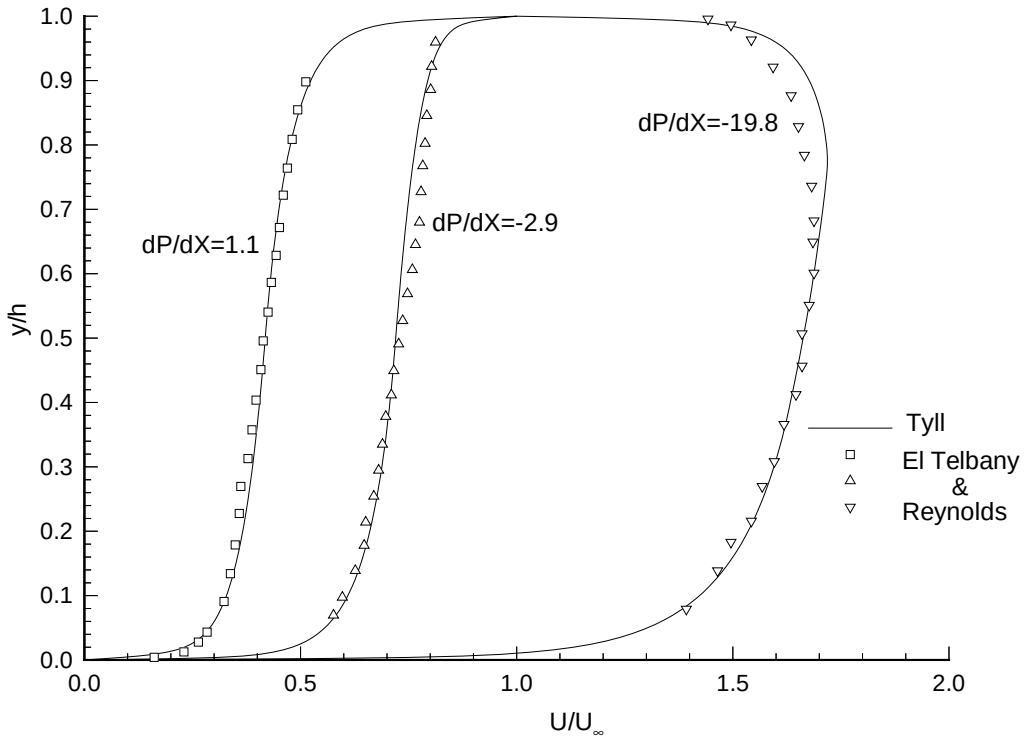

Figure 2.9: Comparison on Analysis and Experiment for Couette/Poiseuille Flow Velocity Profiles [54]

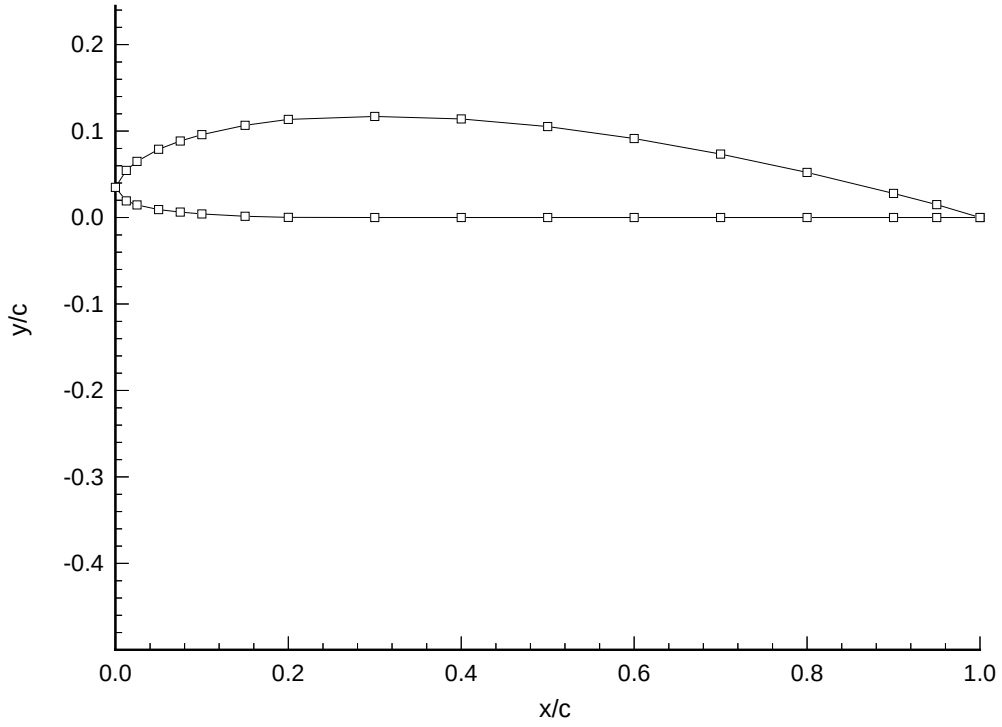

Figure 2.10: Surface Grid of Clark Y Airfoil

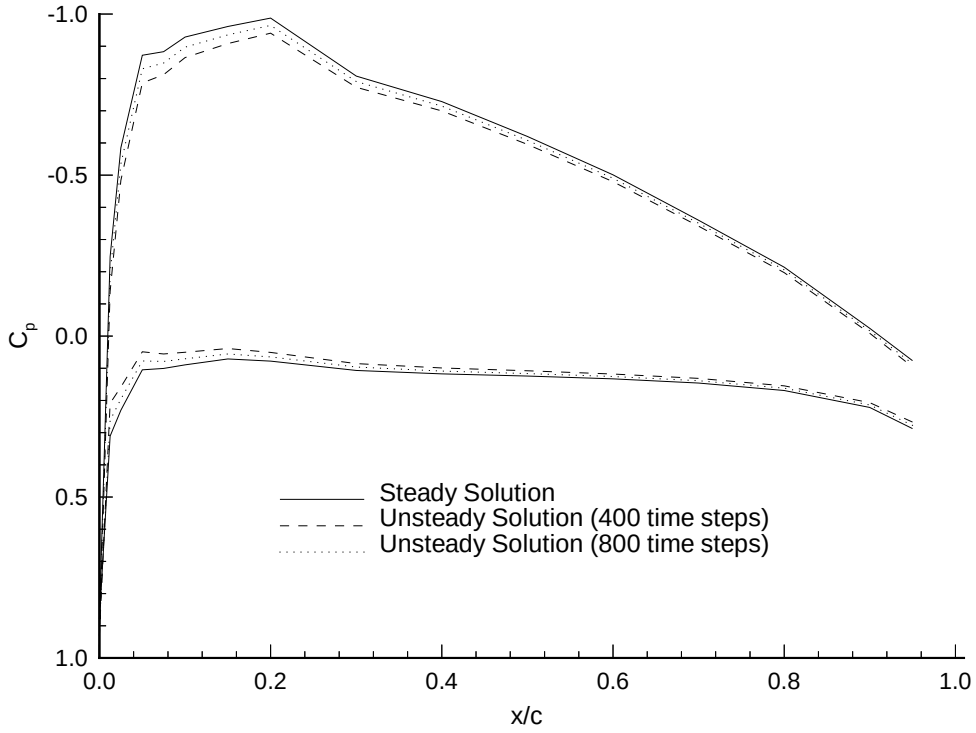

Figure 2.11: Predicted Clark Y Airfoil Pressure Coefficients Using Steady and Unsteady Vortex Panel Methods (Out of Ground Effect)

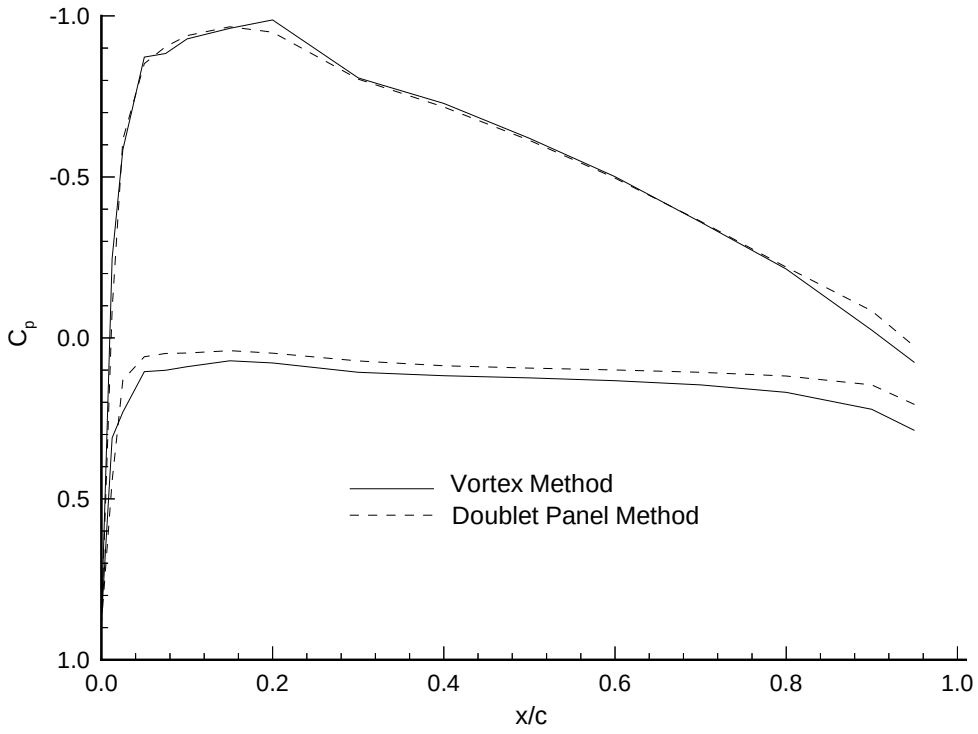

Figure 2.12: Comparison of Doublet Panel Method and Vortex Panel Method Pressure Coefficient Predictions on Clark Y Airfoil Out of Ground Effect

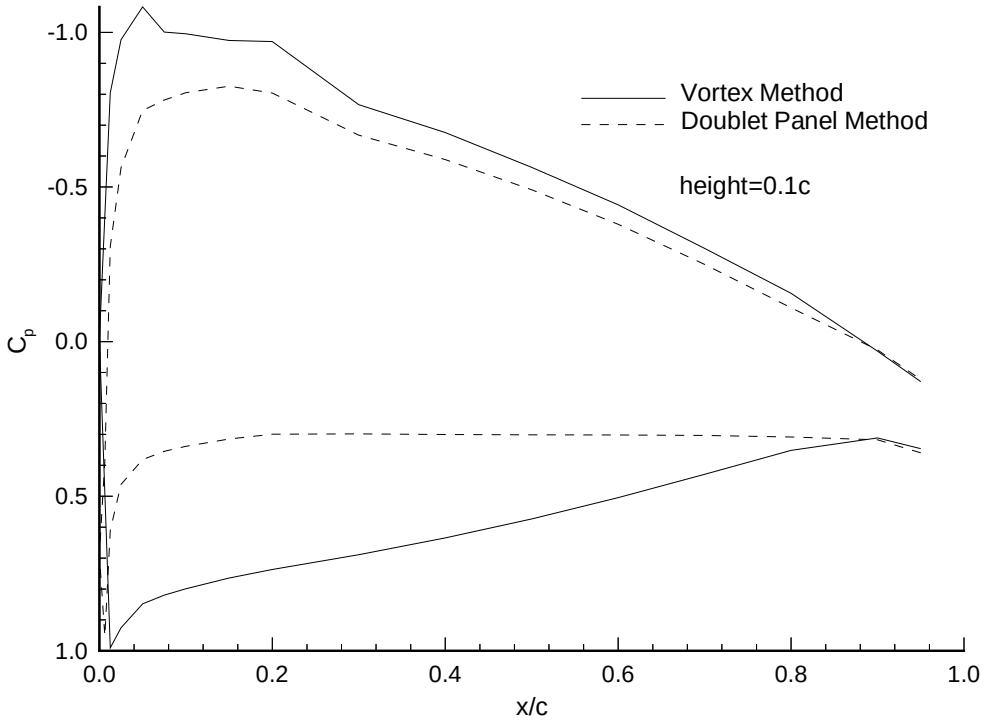

Figure 2.13: Comparison of Doublet Panel Method and Vortex Panel Method Pressure Coefficient Predictions on Clark Y Airfoil In Ground Effect

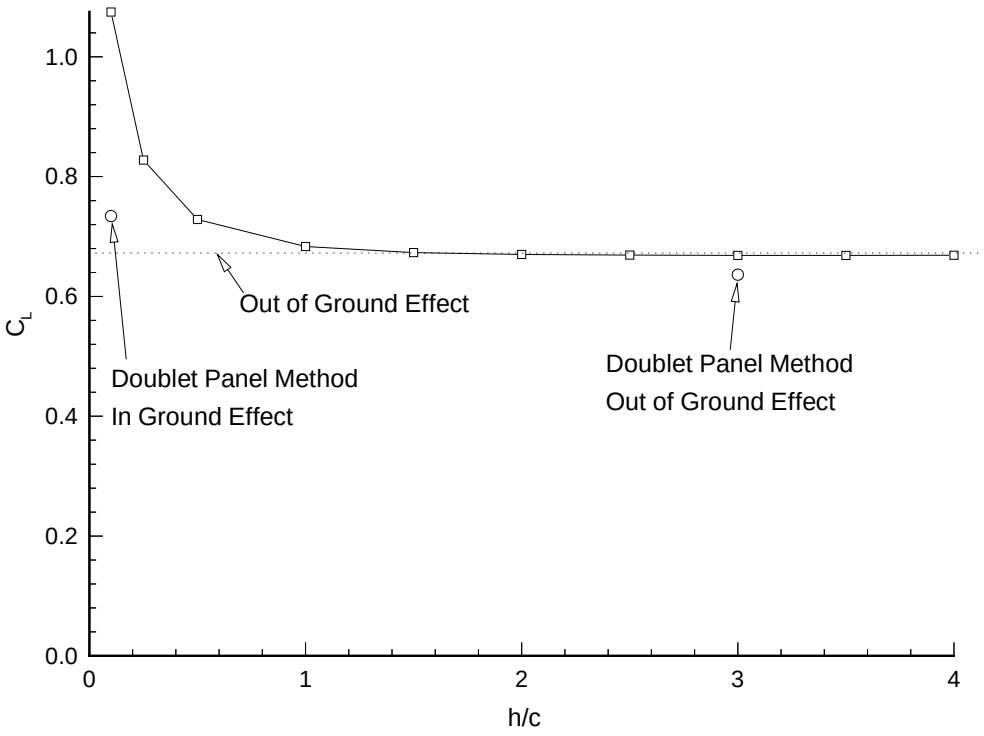

Figure 2.14: Predicted Lift Coefficient vs Height for Clark Y Airfoil Using the Vortex Panel Method

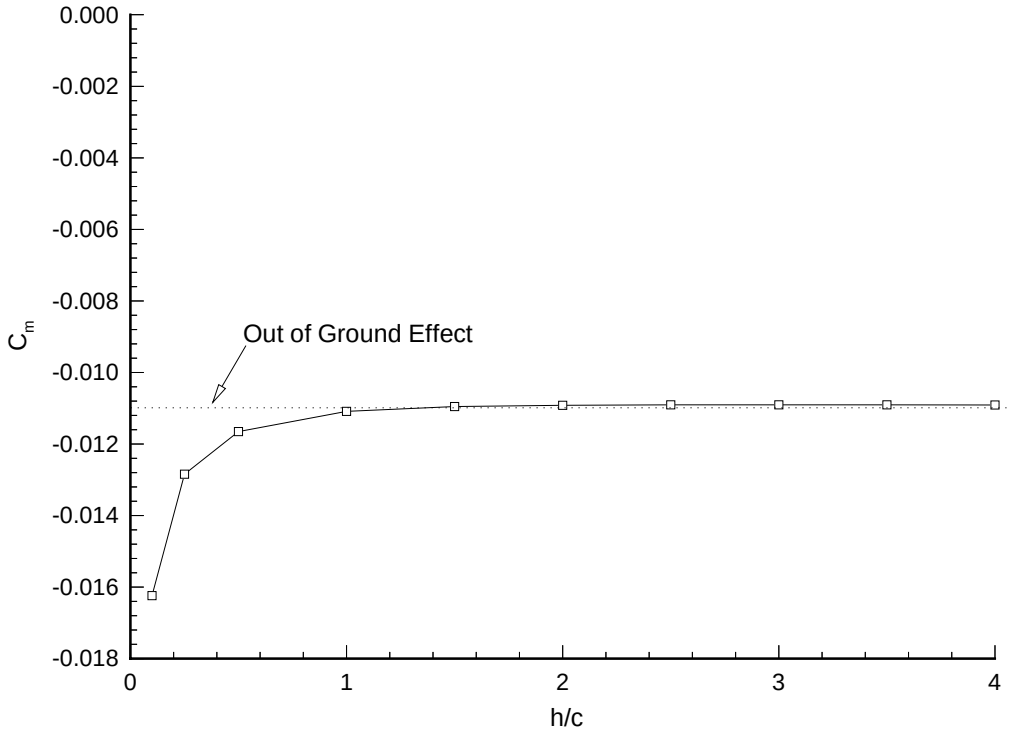

Figure 2.15: Predicted Pitching Moment Coefficient vs Height for Clark Y Airfoil Using the Vortex Panel Method

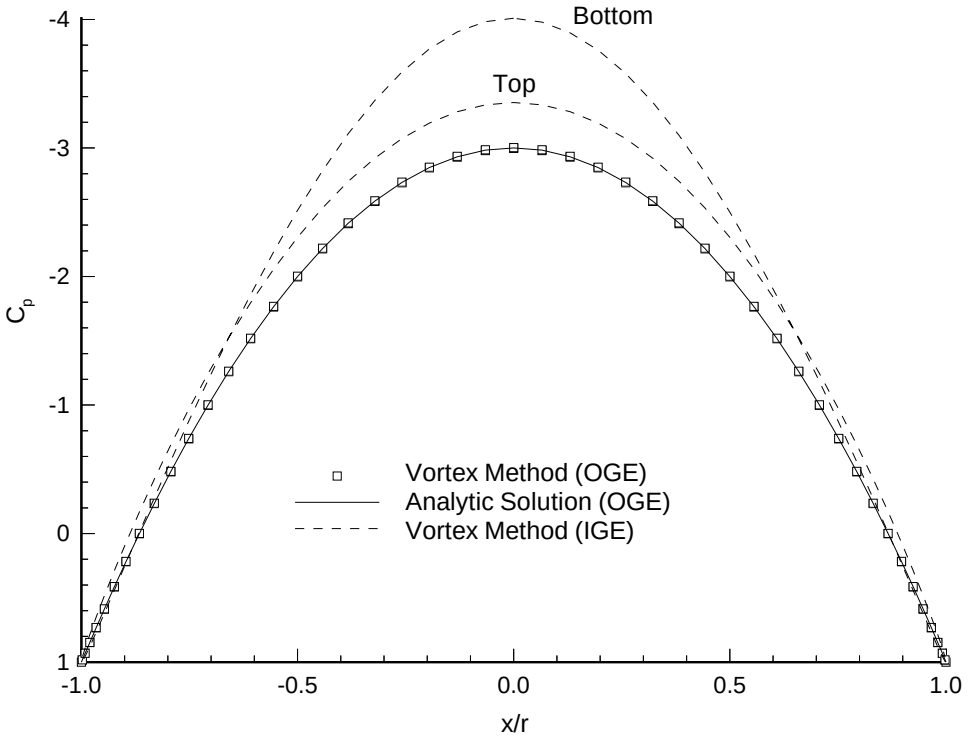

Figure 2.16: Pressure Coefficient Over Circular Cylinder w/o Separation

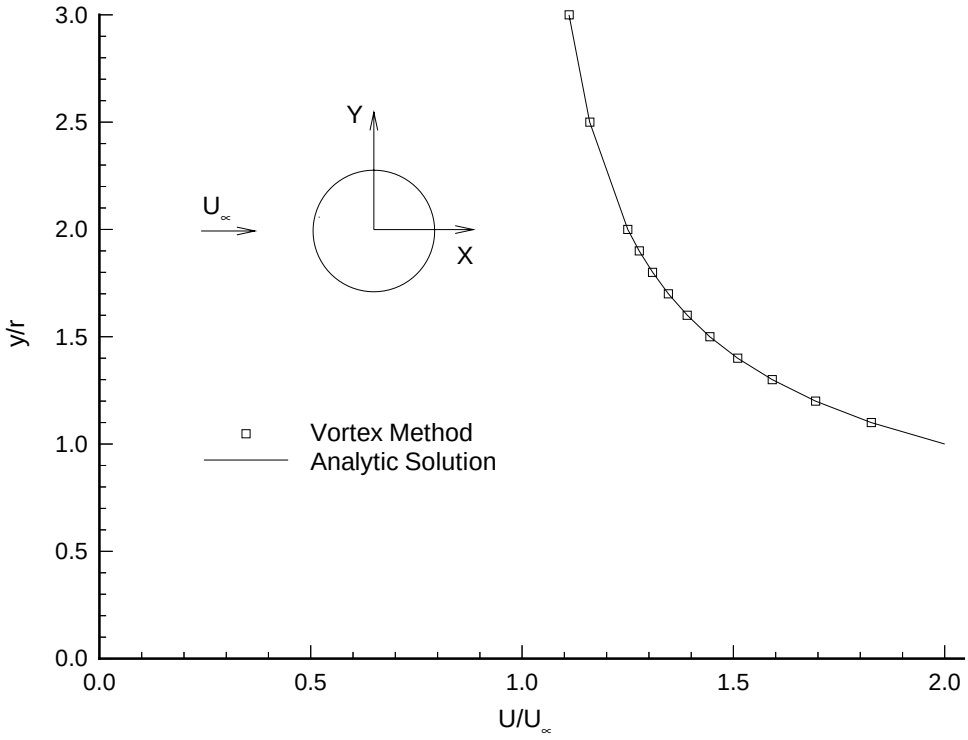

Figure 2.17: Velocity Profile Over Circular Cylinder w/o Separation Top Vertical Centerline, Out of Ground Effect

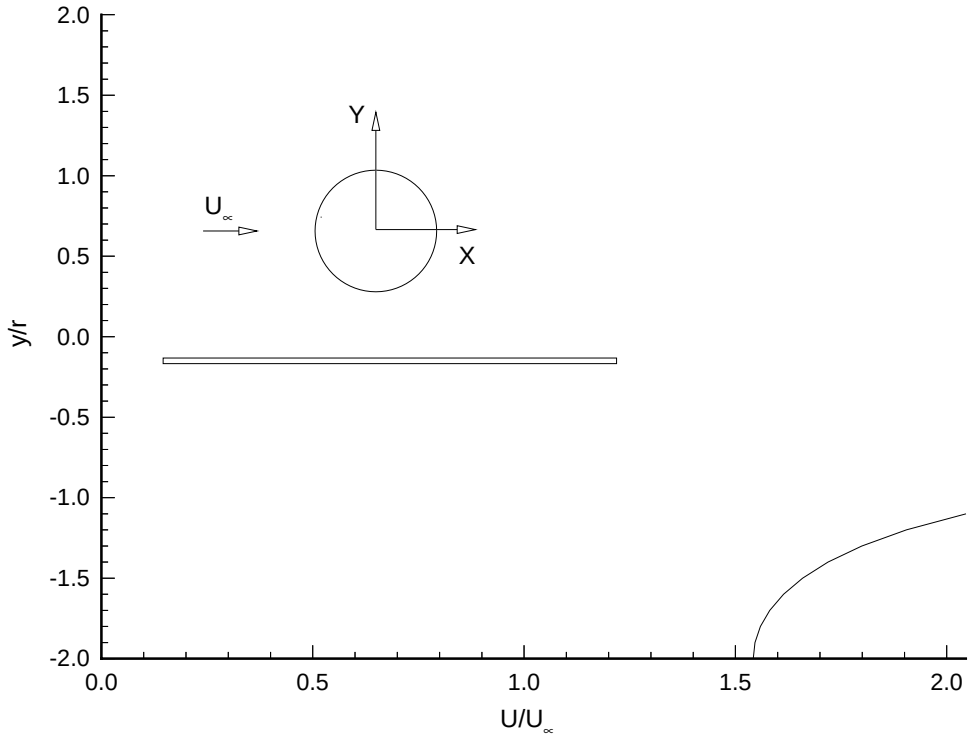

Figure 2.18: Velocity Profile Over Circular Cylinder w/o Separation Bottom Vertical Centerline, In Ground Effect

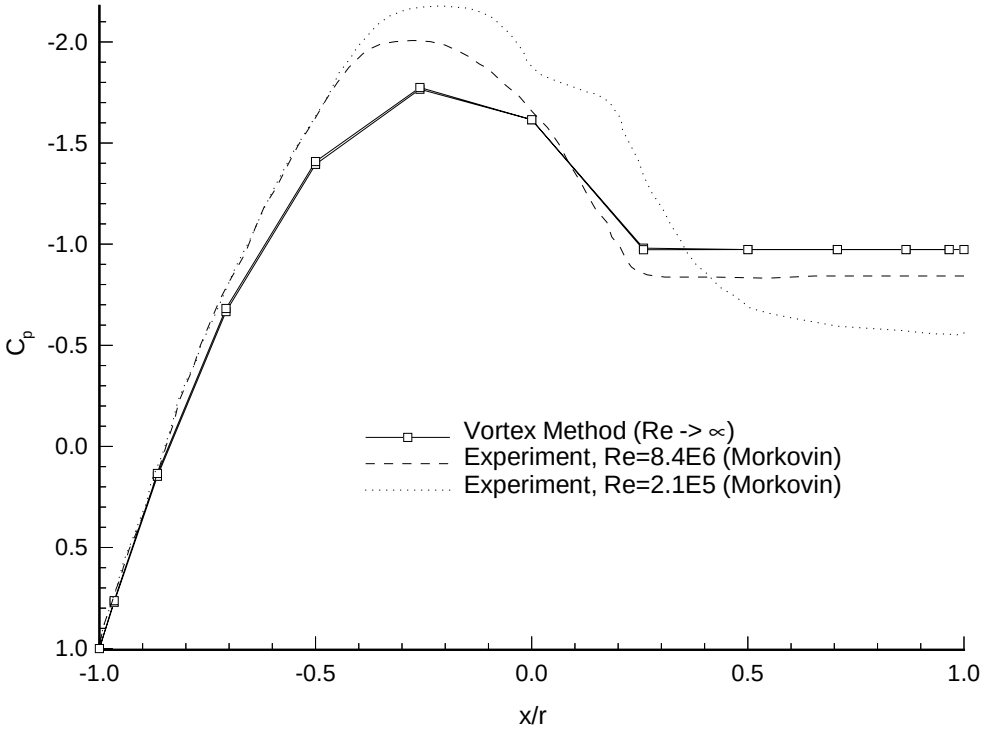

Figure 2.19: Pressure Coefficient Over Circular Cylinder Out of Ground Effect

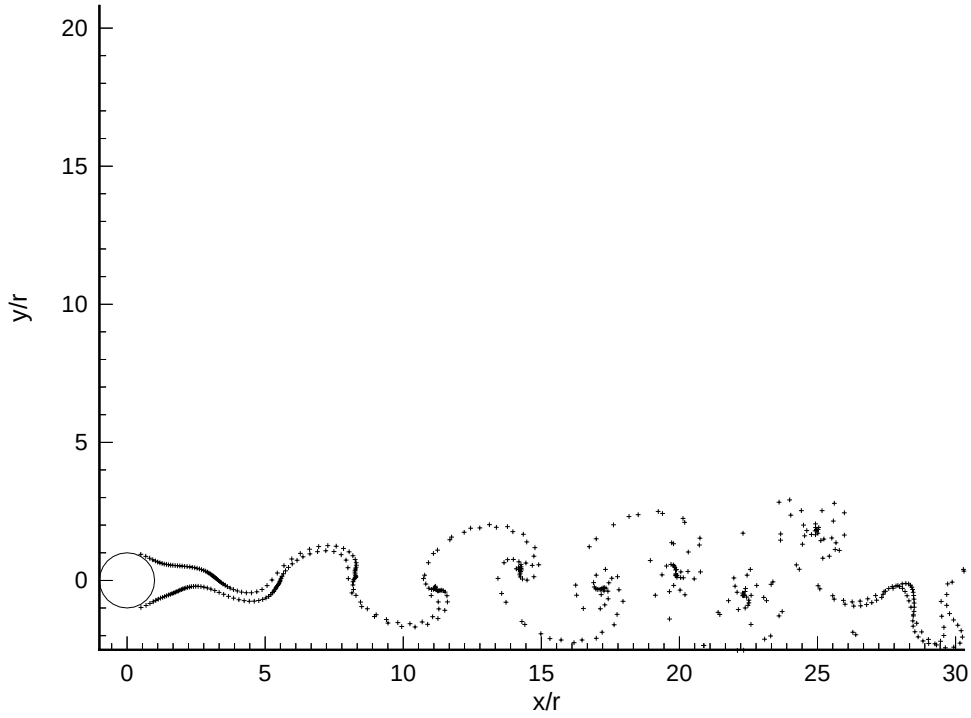

Figure 2.20: Separated Flow Over Circular Cylinder by the Vortex Panel Method

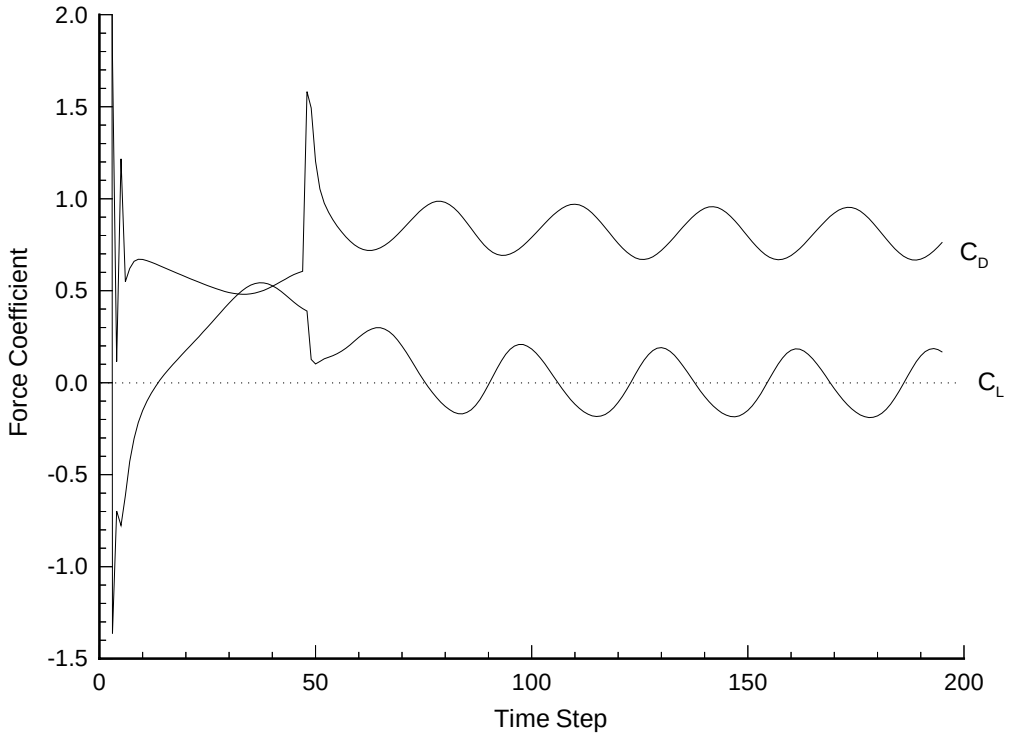

Figure 2.21: Time History of Lift and Drag Coefficient for Circular Cylinder Out of Ground Effect predicted by the Vortex Panel Method

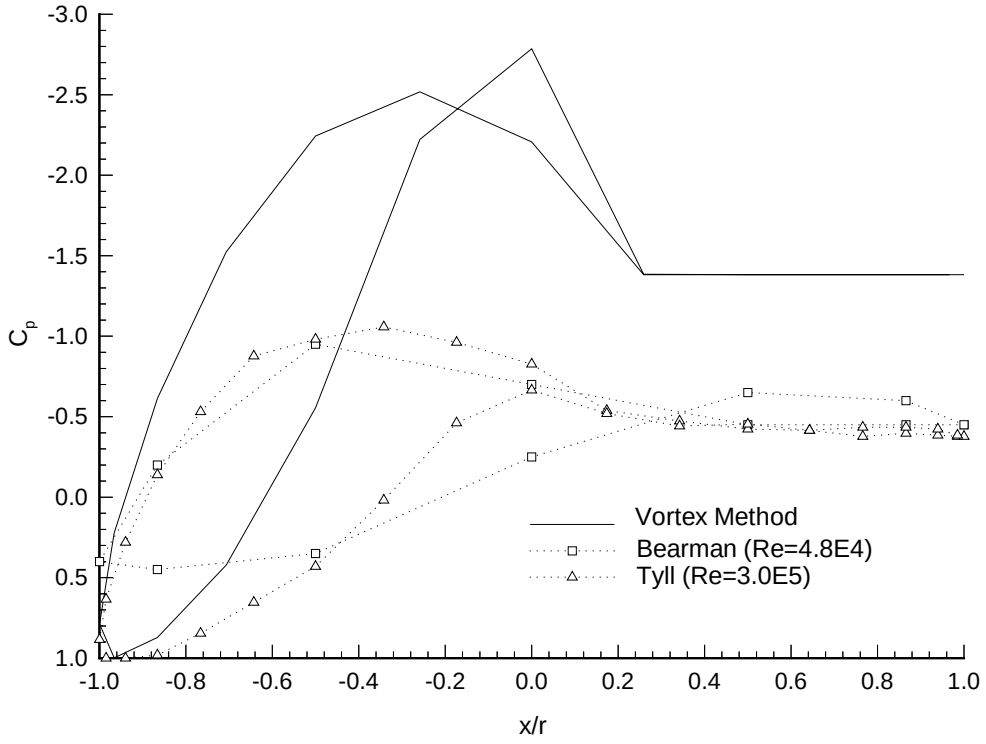

Figure 2.22: Pressure Coefficient Over Circular Cylinder In Ground Effect (h/d=0.1)

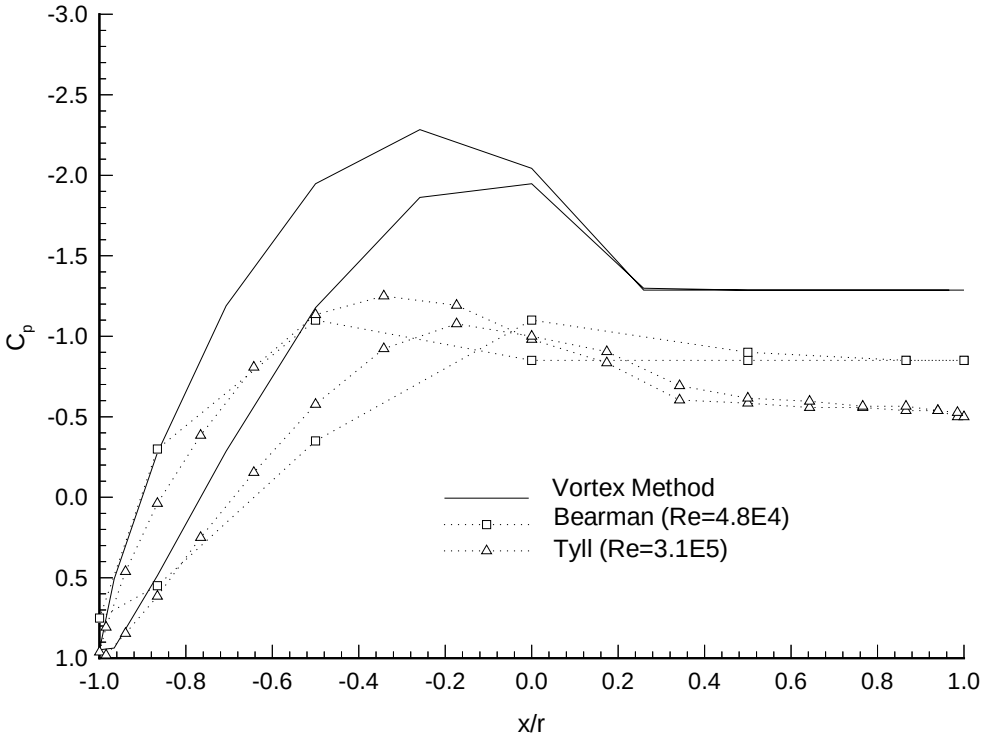

Figure 2.23: Pressure Coefficient Over Circular Cylinder In Ground Effect (h/d=0.4)

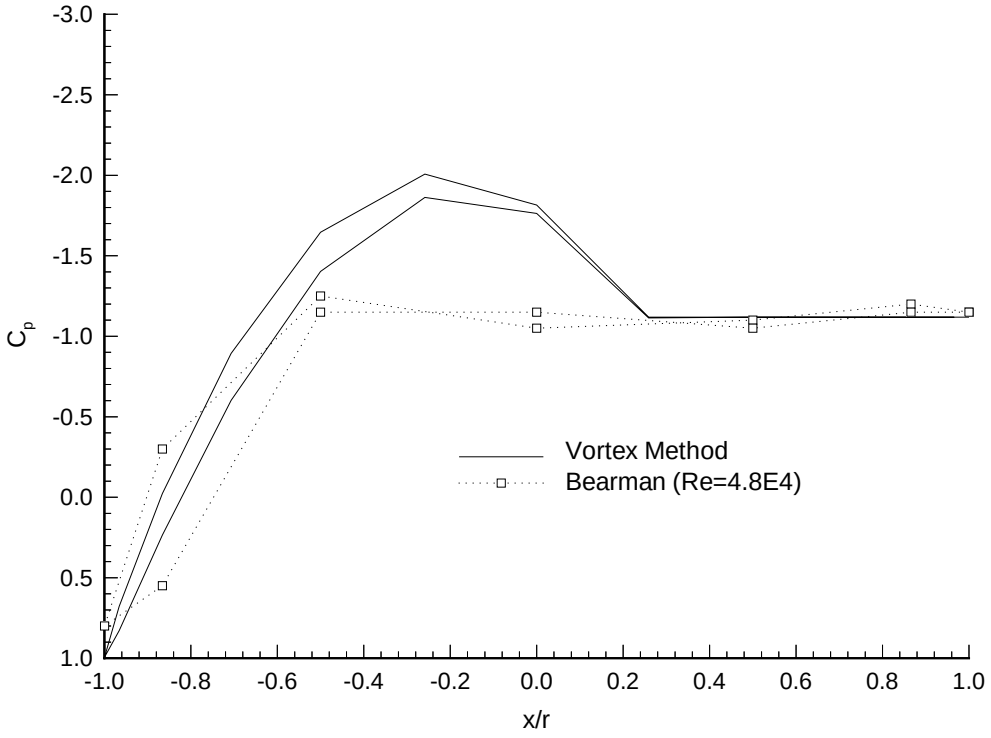

Figure 2.24: Pressure Coefficient Over Circular Cylinder In Ground Effect (h/d=1.0)

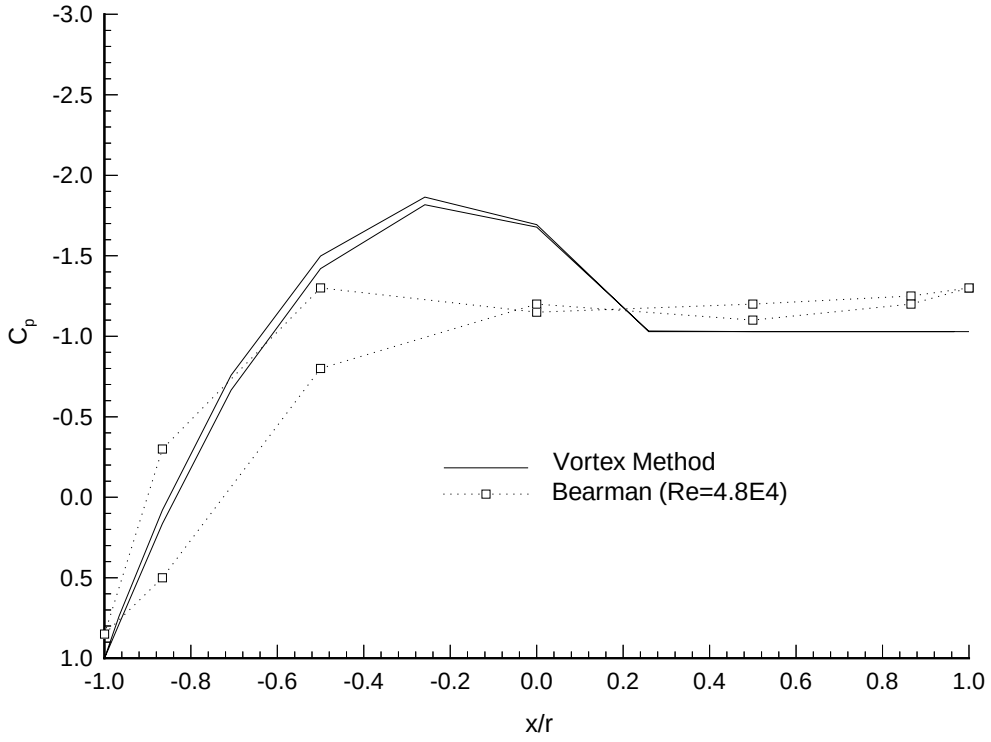

Figure 2.25: Pressure Coefficient Over Circular Cylinder In Ground Effect (h/d=2.0)

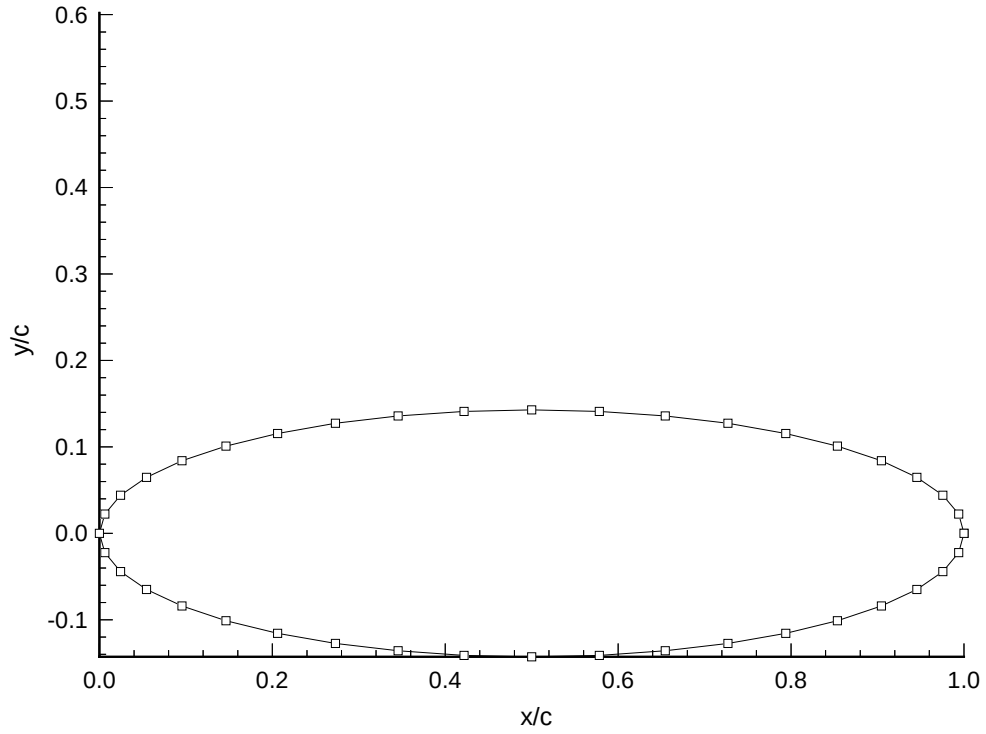

Figure 2.26: Surface Grid of Elliptic Cylinder

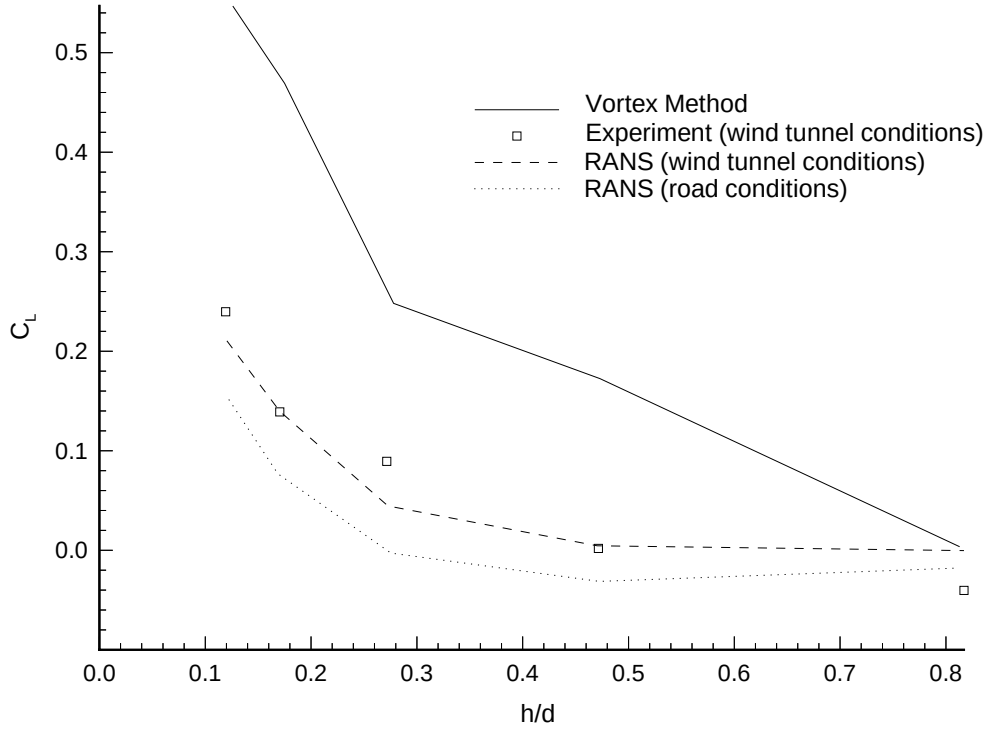

Figure 2.27: Lift Coefficient of a 3.5:1 Elliptic Cylinder vs Height to Width Ratio

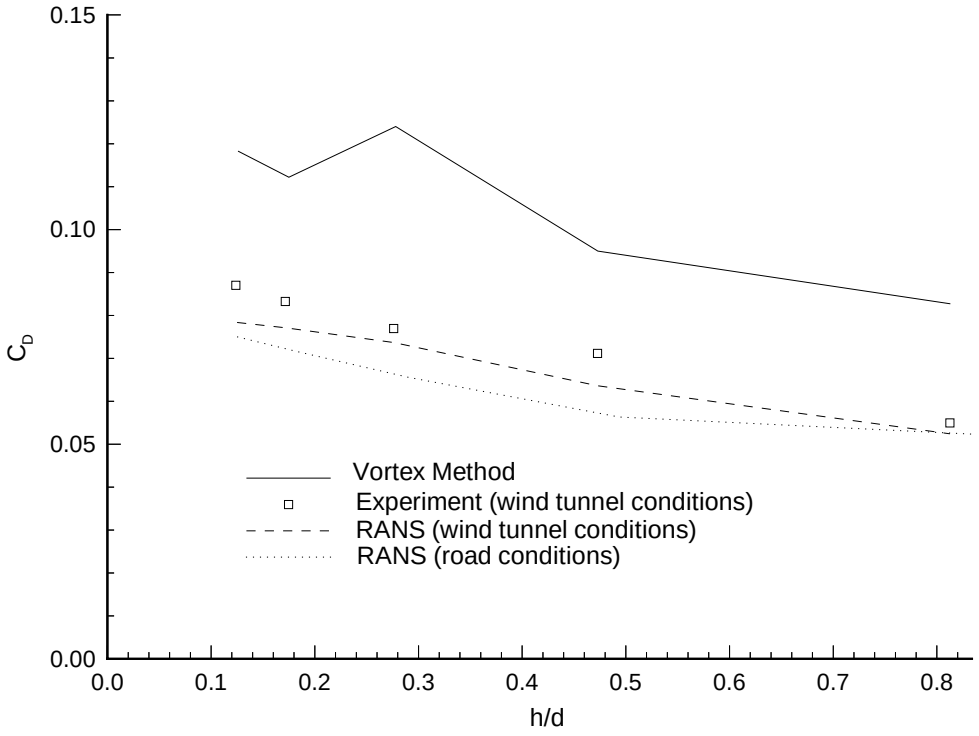

Figure 2.28: Drag Coefficient of a 3.5:1 Elliptic Cylinder vs Height to Width Ratio

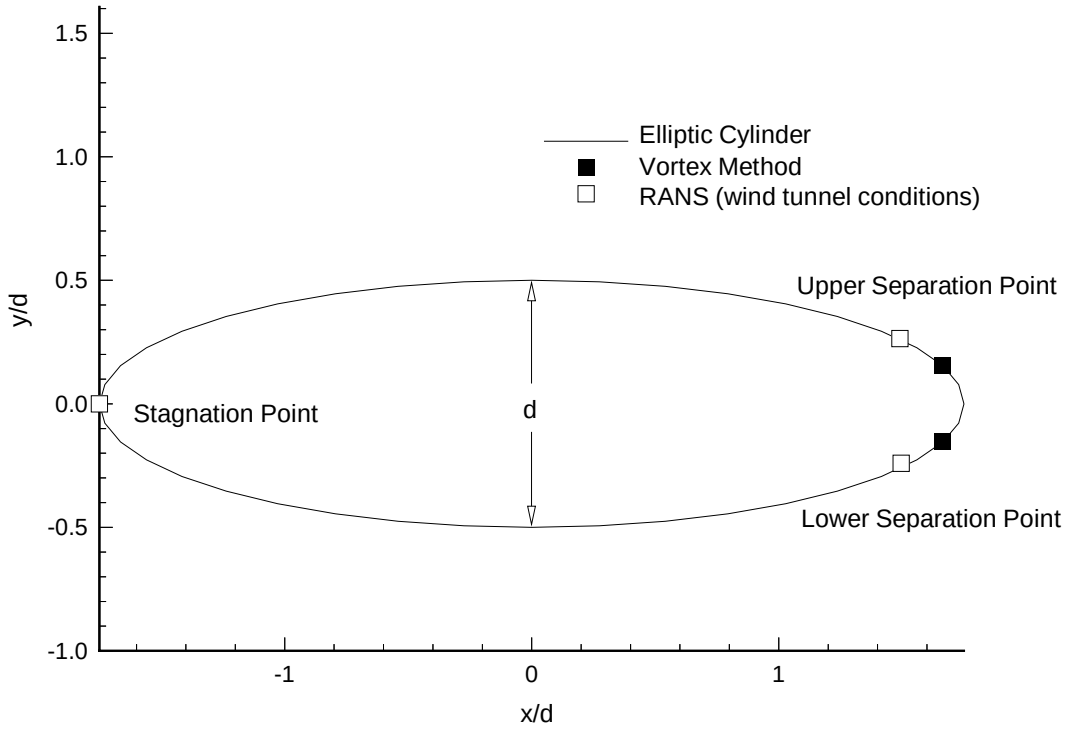

Figure 2.29: Separation and Stagnation Point Locations for Elliptic Cylinder Out of Ground Effect

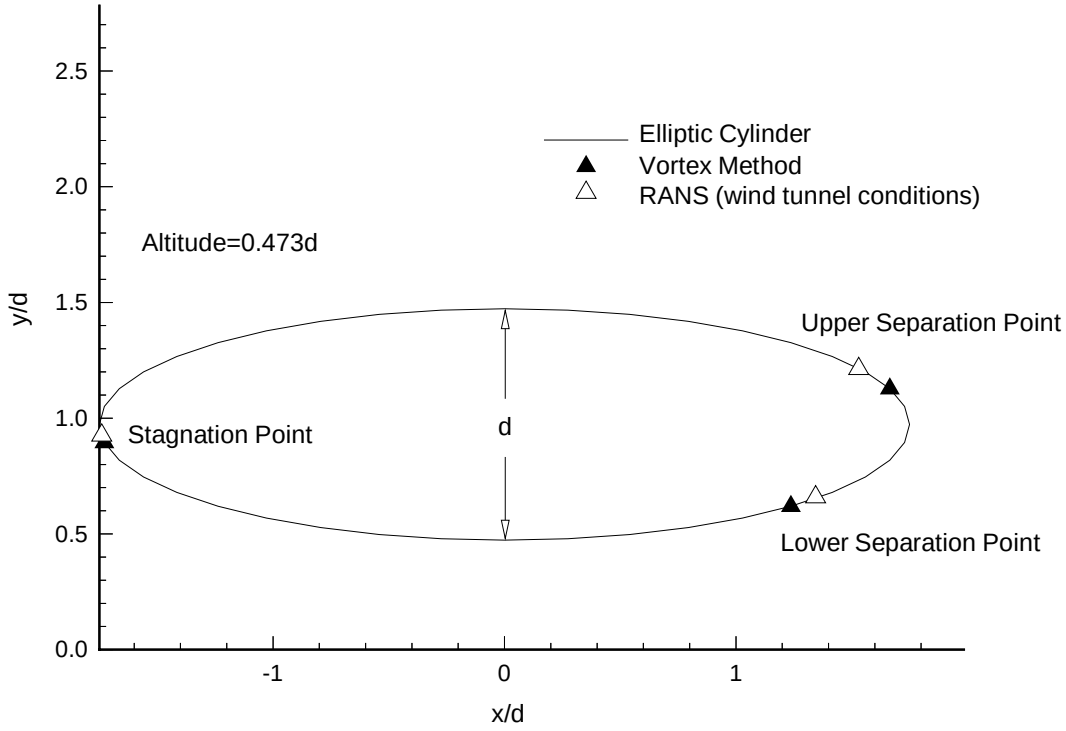

Figure 2.30: Separation and Stagnation Point Locations for Elliptic Cylinder at height-to-diameter ratio of 0.473

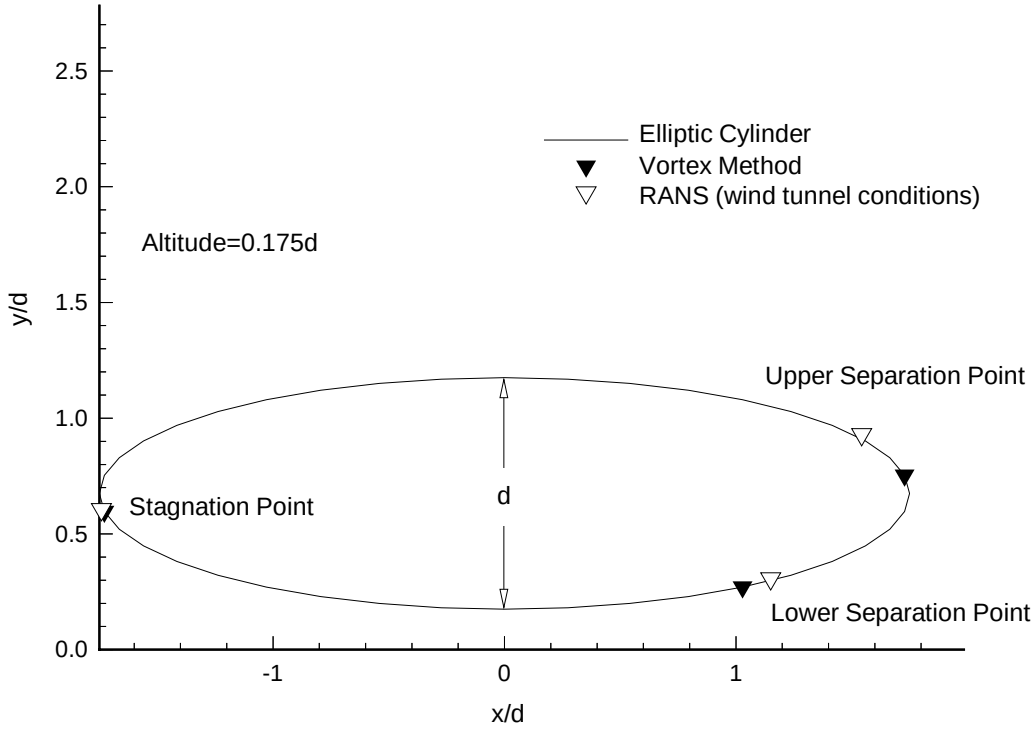

Figure 2.31: Separation and Stagnation Point Locations for Elliptic Cylinder at height-to-diameter ratio of 0.175

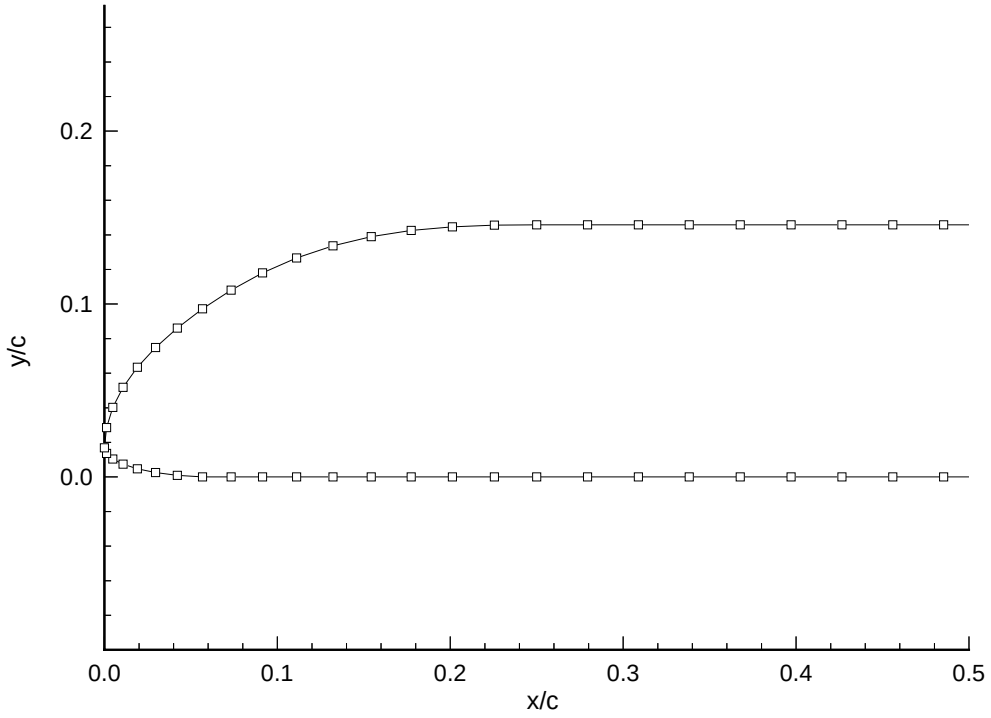

Figure 2.32: Surface Grid for Grumman MAG950

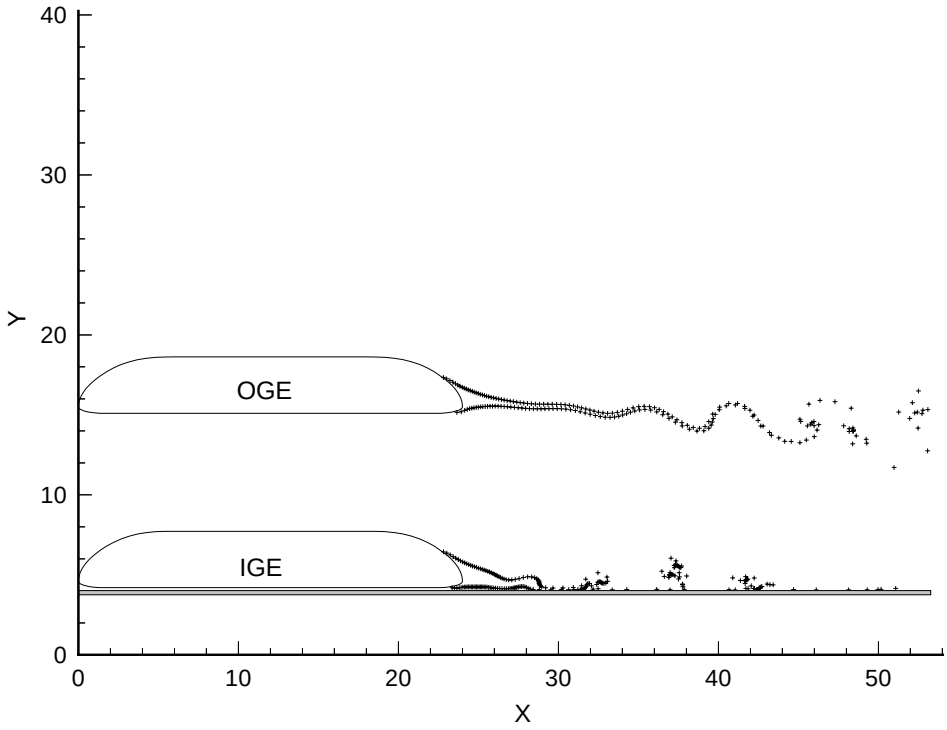

Figure 2.33: Vortex Panel Method Solution for MAG950

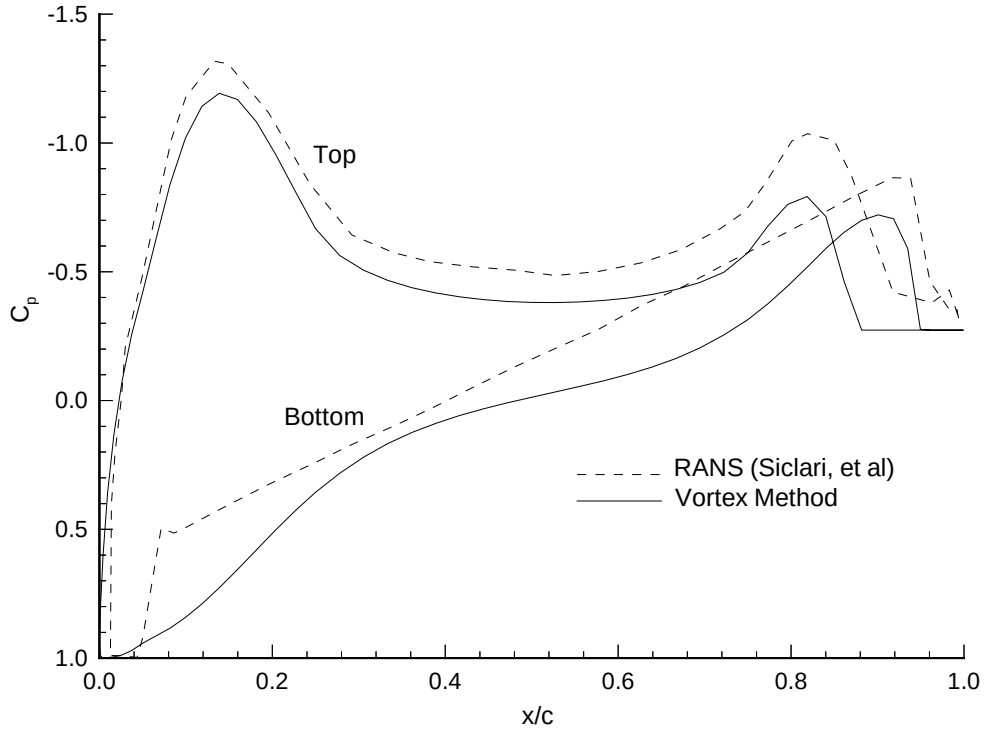

Figure 2.34: Pressure Coefficient over the MAG950 2-D Side View In Ground Effect ($\frac{h}{d} = 0.029$)

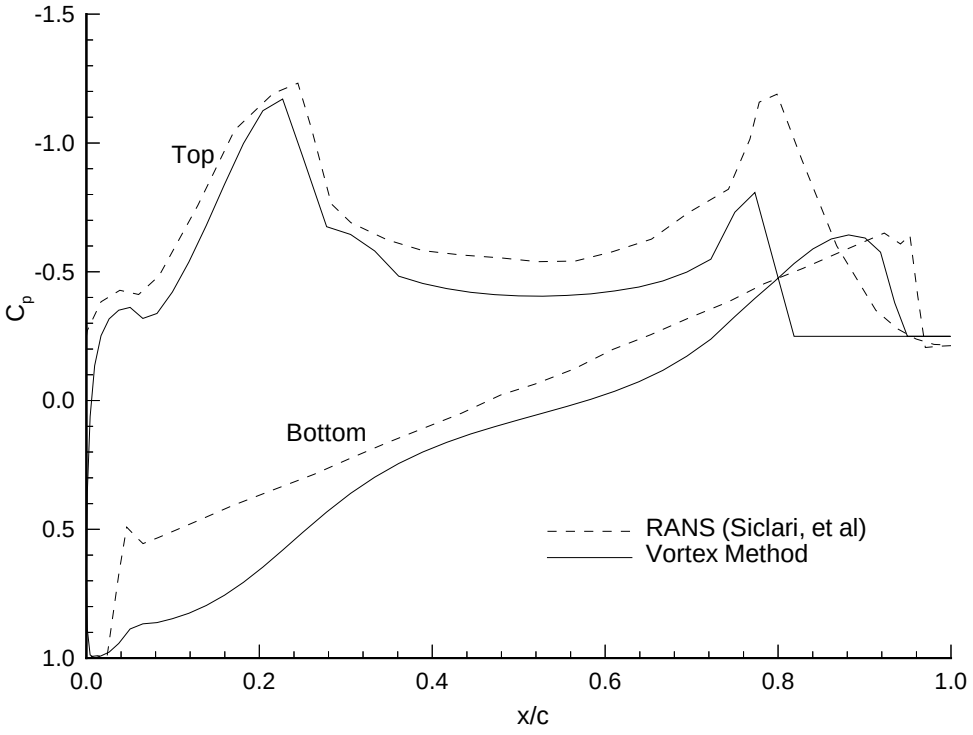

Figure 2.35: Pressure Coefficient over the MAG1002 2-D Side View In Ground Effect ($\frac{h}{d} = 0.029$)

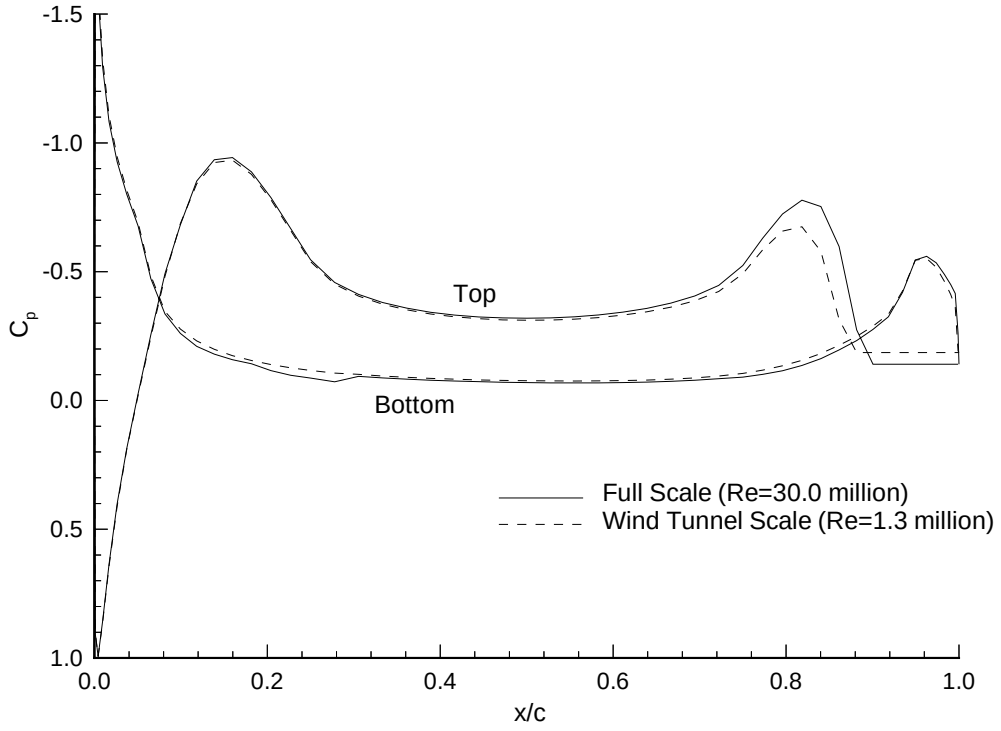

Figure 2.36: Pressure Coefficient for the Full Scale and Wind Tunnel Scale Cases of MAG950 Out of Ground Effect (Vortex Panel Method)

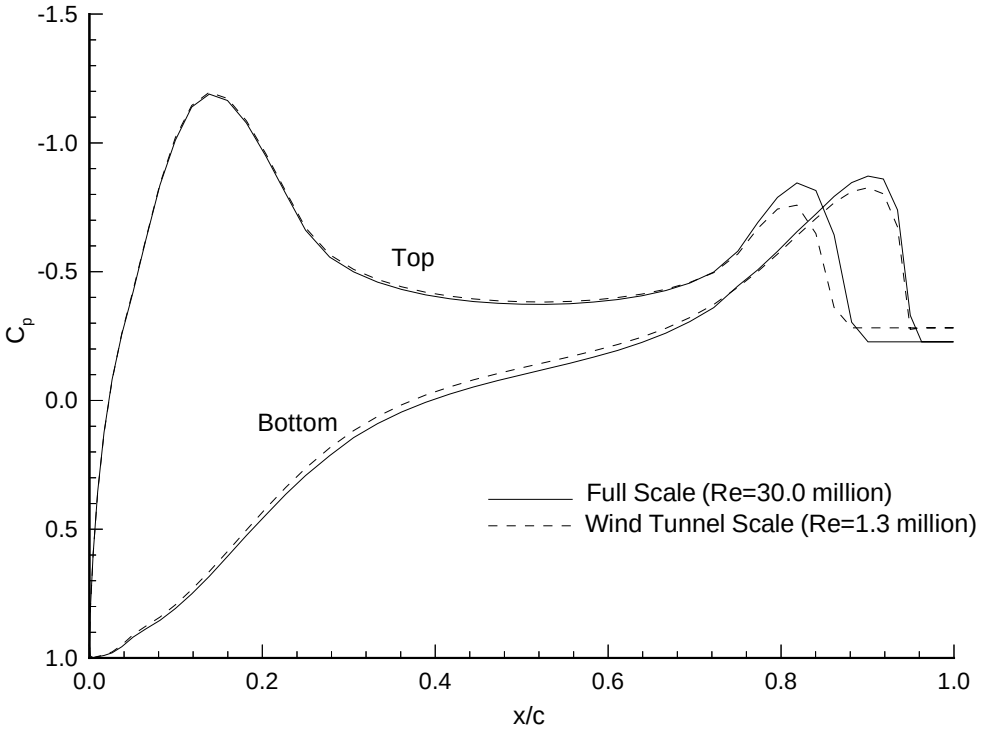

Figure 2.37: Pressure Coefficient for the Full Scale and Wind Tunnel Scale Cases of MAG950 In Ground Effect (Vortex Panel Method)

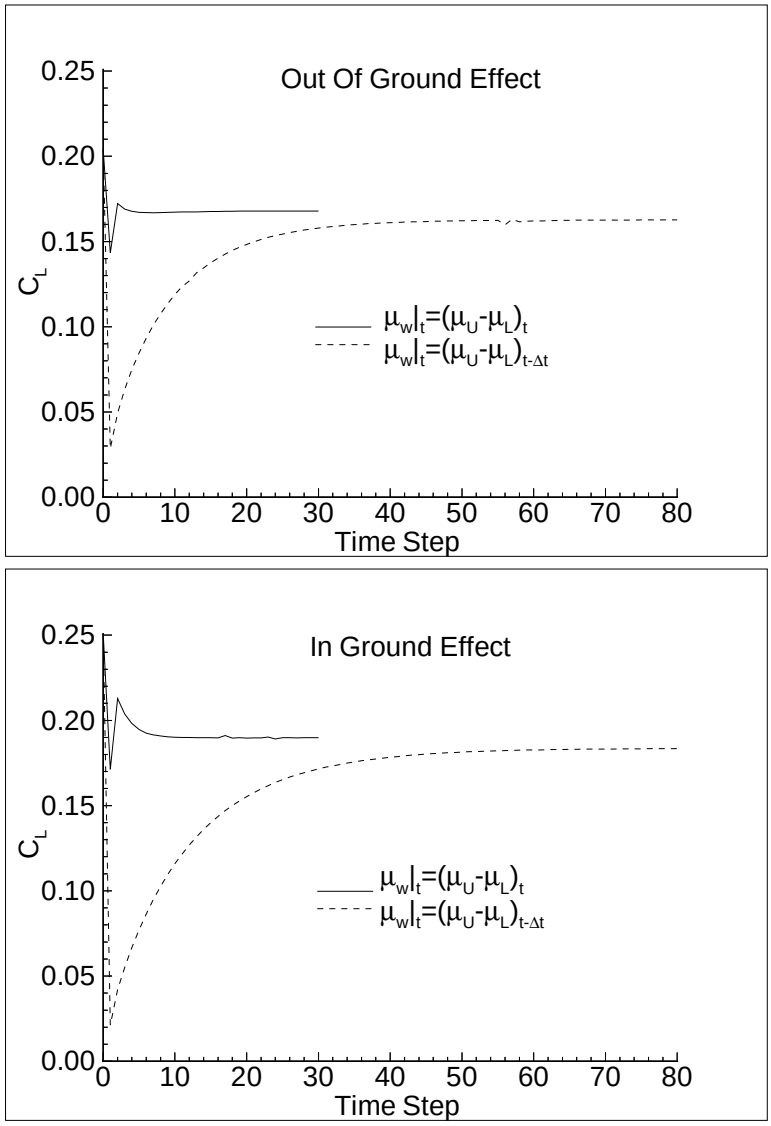

Figure 2.38: Solution Time History for Flow Over a Finite Thickness ClarkY Airfoil (AR=1.0) Out of Ground Effect (Top) and In Ground Effect (Bottom); Doublet Panel Method

Figure 2.39: Flow Over A ClarkY Airfoil (AR=1.0) Out of Ground Effect; Doublet Panel Method

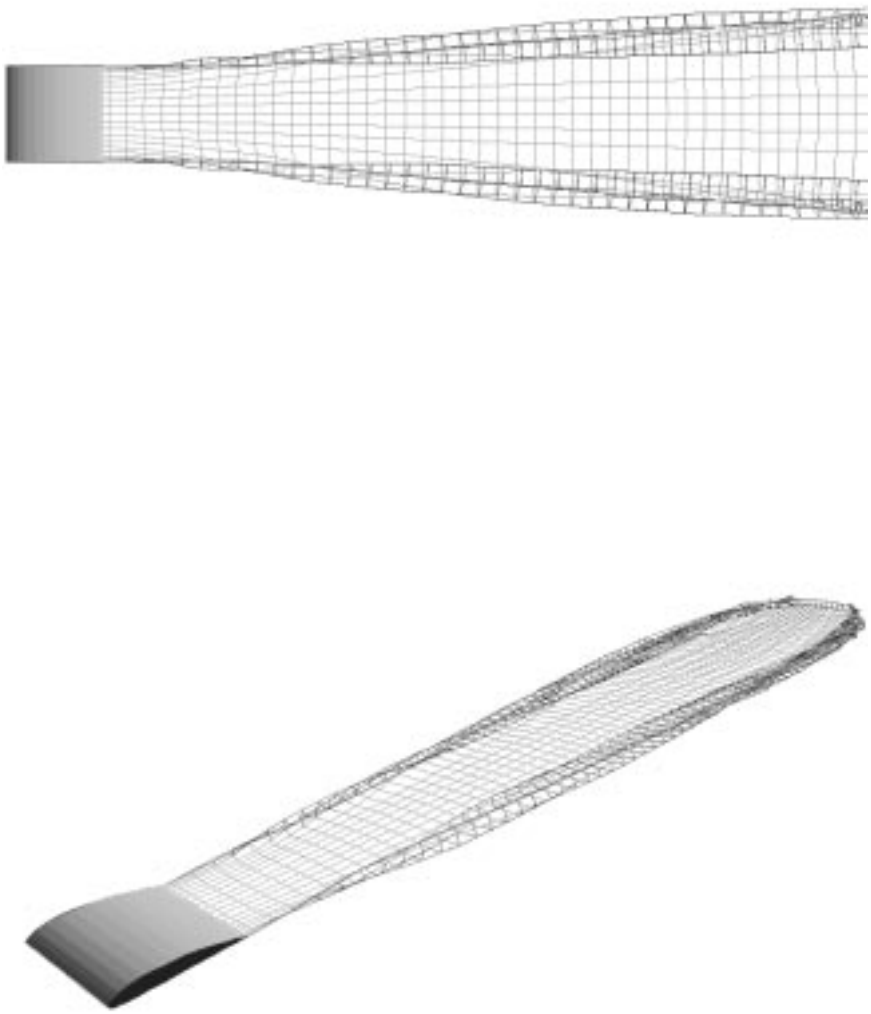

Figure 2.40: Flow Over A ClarkY Airfoil (AR=1.0) In Ground Effect; Doublet Panel Method

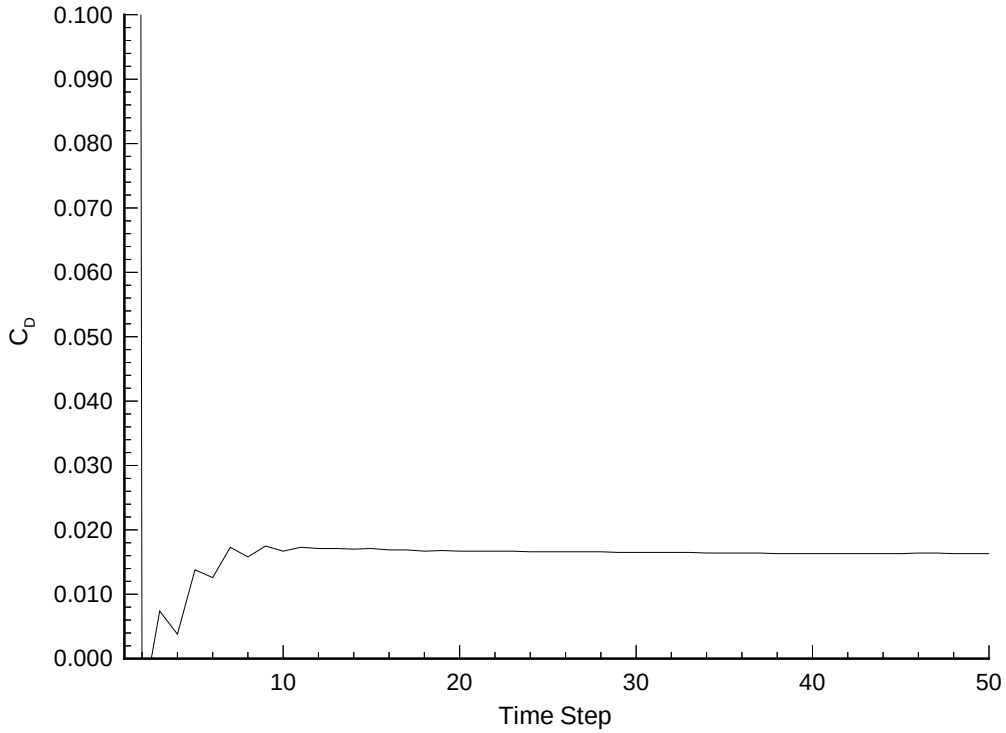

Figure 2.41: Solution Time History for Flow Over a Sphere With Turbulent Separation as Predicted by the Doublet Panel Method

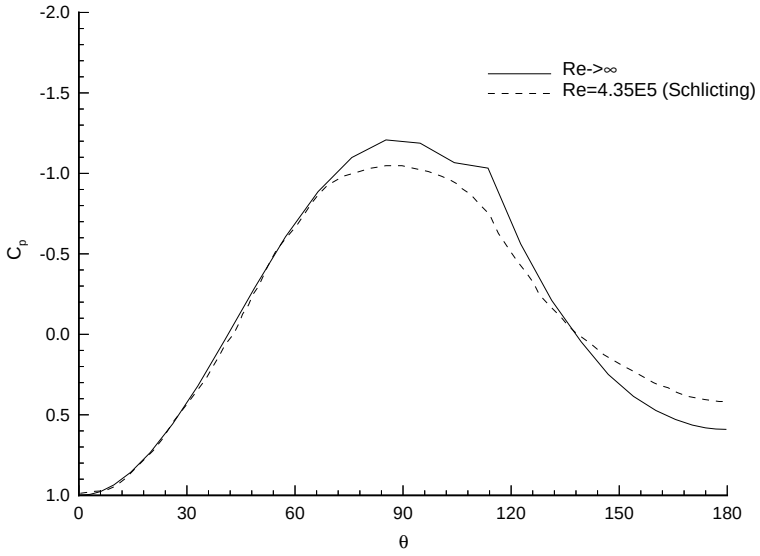

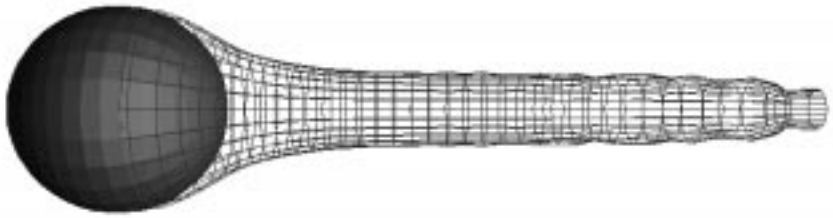

Figure 2.42: Pressure Coefficient for Flow Over a Sphere With Turbulent Separation as Predicted by the Doublet Panel Method (Separation at 104°) [62]

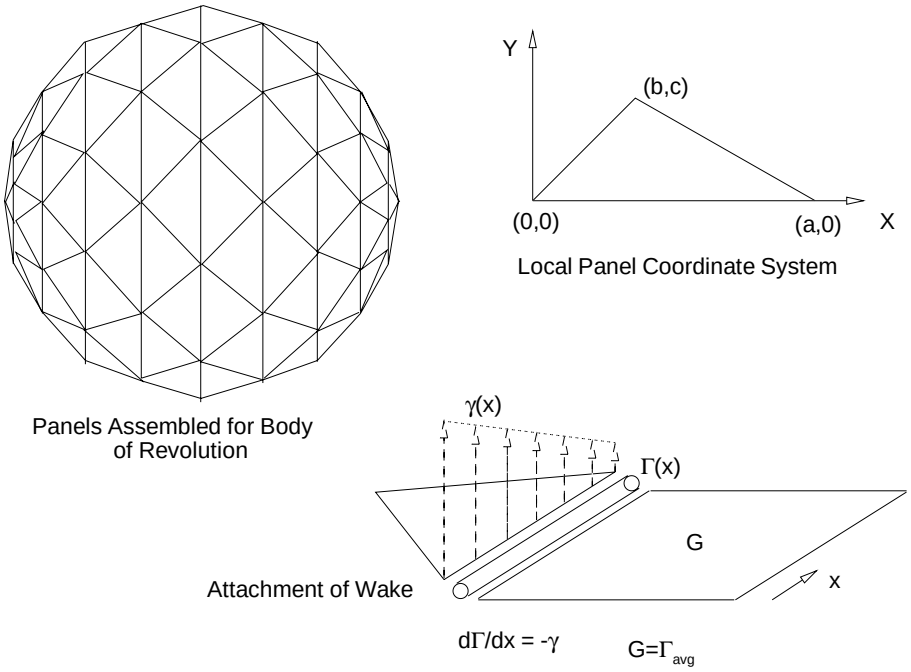

Figure 2.43: 3-D Vortex Panel Method, Panels and Panel Assembly

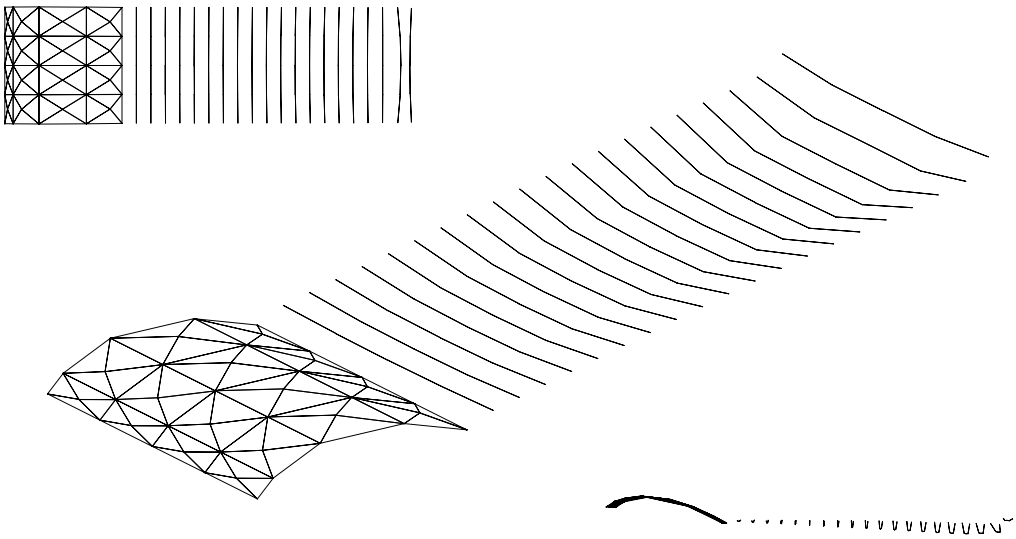

Figure 2.44: Mean Camber Line of ClarkY, Aspect Ratio of 1.0, Out of Ground Effect (Vortex Panel Method)

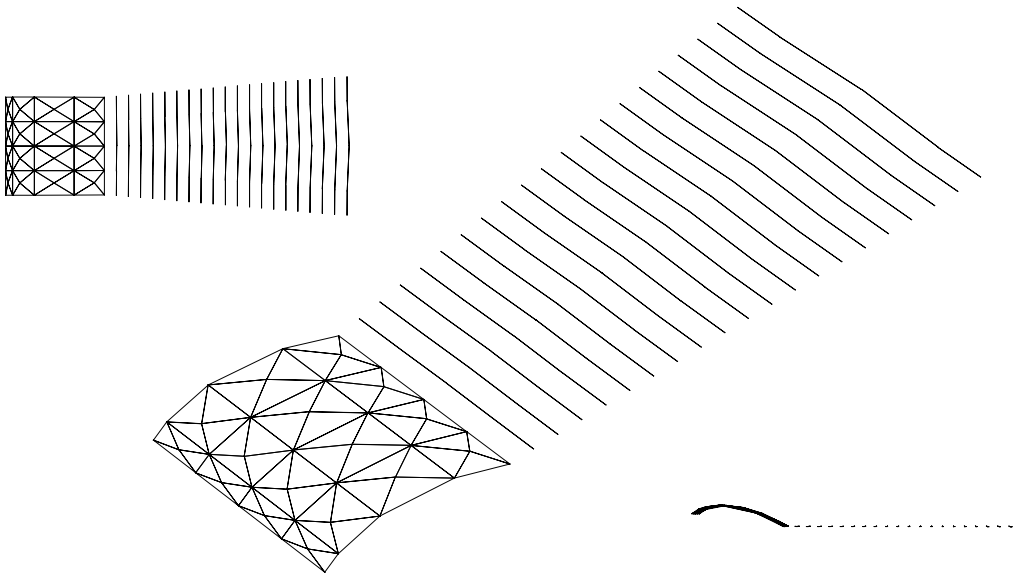

Figure 2.45: Mean Camber Line of ClarkY, Aspect Ratio of 1.0, In Ground Effect (Vortex Panel Method)

Model	C_L	C_D	C_m
MAG950	3.362	0.253	-0.059
MAG1002	3.926	0.217	-0.086
MAG1007	2.683	0.247	-0.027
MAG1742	2.885	0.213	-0.037
MAG1459	3.914	0.053	-0.083

Table 2.1: Force and Moment Coefficients for Northrop Grumman MAGLEV Designs Calculated Using the Vortex Panel Method

Model	OGE	IGE
Base	1.204	3.361
Total	1.202	3.362

Table 2.2: Comparison of In and Out of Ground Effect Lift Coefficients for the Wind Tunnel Scale MAG950 Using the Vortex Panel Method

Model	OGE	IGE
Base	0.131	0.185
Total	0.168	0.253

Table 2.3: Comparison of In and Out of Ground Effect Drag Coefficients for the Wind Tunnel Scale MAG950 Using the Vortex Panel Method

	Wind Tunnel Scale	Full Scale
C_L	1.202	1.413
C_D	0.168	0.147

Table 2.4: A Comparison of Wind Tunnel Scale and Full Scale Force Coefficient Predictions for the MAG950, Out of Ground Effect Using the Vortex Panel Method

	Wind Tunnel Scale	Full Scale
C_L	3.362	3.461
C_D	0.253	0.203

Table 2.5: A Comparison of Wind Tunnel Scale and Full Scale Force Coefficient Predictions for the MAG950, In Ground Effect Using the Vortex Panel Method